Experimental parameter study for passive vortex generators on a 30% thick airfoil

Baldacchino, Daniel; Ferreira, Carlos; De Tavernier, D.A.M.; Timmer, W. A.; van Bussel, G. J.W.

DOI
10.1002/we.2191

Publication date
2018

Document Version
Final published version

Published in
Wind Energy

Received: 30 May 2017 | Revised: 5 February 2018 | Accepted: 6 February 2018
DOI: 10.1002/we.2191

WILEY

RESEARCH ARTICLE

Experimental parameter study for passive vortex generators on a 30% thick airfoil

Daniel Baldacchino | **Carlos Ferreira** | **Delphine De Tavernier** | **W.A. Timmer** | **G. J. W. van Bussel**

Wind Energy Section, Faculty of Aerospace Engineering, Delft University of Technology, Kluyverweg 1, 2629HS Delft, The Netherlands

Correspondence
Daniel Baldacchino, Wind Energy Section, Faculty of Aerospace Engineering, Delft University of Technology, Kluyverweg 1, 2629HS Delft, The Netherlands.
Email: daniel.baldacchino@alumni.um.edu.mt

Funding information
EU's FP7 AVATAR, Grant/Award Number: 608396; Dutch TKI Wind op Zee D4REL, Grant/Award Number: TKIW02007

Abstract

Passive vane–type vortex generators (VGs) are commonly used on wind turbine blades to mitigate the effects of flow separation. However, significant uncertainty surrounds VG design guidelines. Understanding the influence of VG parameters on airfoil performance requires a systematic approach targeting wind energy-specific airfoils. Thus, the 30%-thick DU97-W-300 airfoil was equipped with numerous VG designs, and its performance was evaluated in the Delft University Low Turbulence Wind Tunnel at a chord-based Reynolds number of 2×10^6. Oil-flow visualizations confirmed the suppression of separation as a result of the vortex-induced mixing. Further investigation of the oil streaks demonstrated a method to determine the vortex strength. The airfoil performance sensitivity to 41 different VG designs was explored by analysing model and wake pressures. The chordwise positioning, array configuration, and vane height were of prime importance. The sensitivity to vane length, inclination angle, vane shape, and array packing density proved secondary. The VGs were also able to delay stall with simulated airfoil surface roughness. The use of the VG mounting strip was detrimental to the airfoil's performance, highlighting the aerodynamic cost of the commonly used mounting technique. Time-averaged pressure distributions and the lift standard deviation revealed that the presence of VGs increases load fluctuations in the stalling regime, compared with the uncontrolled case.

KEYWORDS

DU97W300, passive flow control, parametric study, separation delay, vane type, vortex generators

1 | INTRODUCTION

1.1 | Background

The presence of separated flow on pitch-regulated wind turbine blades is undesirable and degrades performance. Specifically, this may manifest itself as lower annual energy production, higher fatigue loads, and stall noise.[1,2] Inboard blade flows are particularly prone to separation since structural constraints result in thicker root airfoil sections and high local angles of attack, posing stronger adverse pressure gradients (APGs). Vortex generators (VGs) can effectively decrease this APG, improving the pressure recovery over the airfoil and thus delay separation.[3] A typical passive VG is a vane protruding from the surface, angled to the incoming flow, as visualized in Figure 1. Similar to a delta wing system (see, eg, Hoerner[4]), a leading edge vortex develops along the vane and is shed near the tip, creating a wake of upwash and downwash regions. This re-energizes the boundary layer with the outer flow and delays flow reversal (separation).[5]

The simplicity and robustness of VGs have, over time, led to their widespread commercial adoption. Sullivan[6] documented pioneering wind turbine field experiments with VGs in the 1980s with the stall-regulated MOD-2 turbine, followed by the ELKRAFT[7] and AWT-26 machines.[8] These

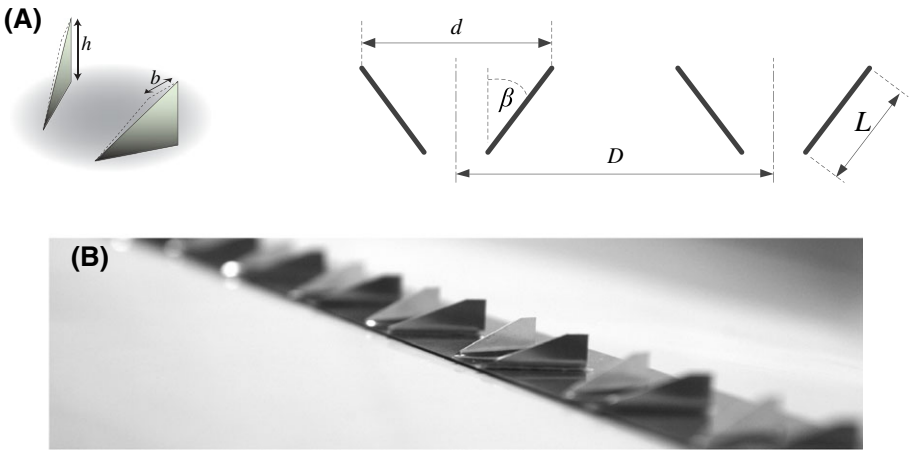

FIGURE 1 A, Isometric view (left) and planar (right) schematic of the periodic vortex generator–array arrangement. B, Mounted cropped-delta vortex generators. Nomenclature: *h*, vane height; *b*, cropped edge length; *d*, intravane spacing; *D*, intervane spacing; β, geometric vane inflow angle; *L*, vane length [Colour figure can be viewed at wileyonlinelibrary.com]

experiments revealed annual energy production gains of 4% to 10%, but at the cost of moderately higher dynamic loads. In fact, in 2D airfoil wind tunnel tests with and without flow control, Griffin[8] (and recently Manolesos and Voutsinas[9]) observed sharper stall onset with VGs, suggesting a more vigorous stall mechanism with VGs. Operational characteristics in the stall regime with VG control have since been seldom addressed in reported literature. A corotating (CoR) array with delta-shaped vanes was chosen for the field tests, but counter-rotating (CtR) VGs performed equally well in the wind tunnel tests. Moreover, these early studies demonstrated that VGs could be used to mitigate roughness-induced performance degradation.

Fundamental and applied investigations in the decades since have shed light on the flow mechanisms and design methologies of VGs. The vortex system produced by a vane or array is primarily described by the vortex strength (Γ), trajectory, and decay rate, which have been used by some authors to indirectly assess the effectiveness of VG designs.[10,11] Jones[10] developed a potential flow model for the vortex kinematics resulting from CtR arrays. Experimental measurements on flat-plate boundary layers have shown good agreement with Jones' model[10] and even extended its use to account for vortex decay[12] and asymmetry.[13] The model inspired Pearcey's[11] detailed discussion of a VG design methodology, proposing optimization objectives that maximize (i) the vortex near-wall residence time and/or circulation per unit span or (ii) the lift gain achievable. The first determines the array effectiveness, the extent of the backflow region that can be controlled, whereas the second pertains to the array efficiency. For example, CtR VGs with common upwash (CU) proved ineffective compared with a common downwash (CD) arrangement because of premature vortex ejection, ie, low near-wall residence time.[11] Lögdberg et al[14] also distinguished these 2 design objectives and further demonstrated that a system optimized for efficiency is not necessarily the most robust.

Wendt[15] further characterized the vortex circulation and flow topology for different rectangular, aerodynamically profiled VGs. The vortex strength increased linearly with the vane angle for $\beta \leq 20^\circ$. Similar trends were seen for the normalized vane height (h/δ), where δ is the boundary layer thickness, as well as the vane aspect ratio (L/h). Furthermore, Angele and Muhammad-Klingmann[16] and Lögdberg et al[14] showed for different VG pairs and arrays that Γ varied in proportion to hU_{VG}, where U_{VG} is the streamwise velocity at the VG tip position. This relation was previously assumed from thin-airfoil theory and deployed in numerous VG models.[10,17]

Ashill et al[17] and Lin[18] demonstrated the effectiveness of submerged ($h/\delta < 1$) VGs, which introduce lower device drag compared with conventional VGs. Godard and Stanislas[19] optimized a submerged VG array for separation prevention in a wind tunnel test section with a tailored APG and evaluated effectiveness in terms of the increase in skin friction. In this sense, the optimal array consisted of CtR delta vanes, with vane angles of $\pm 18^\circ$ and $h/\delta = 0.37$. The performance proved insensitive to the vane length for $L > 3h$. The authors stressed the lower tolerance of submerged devices to changing flow conditions.

In a comprehensive review, Lin[18] described vane shape variants, including rectangular, triangular (delta), and trapezoidal (cropped-delta [CDA]) profiles. These devices were the preferred choice in low-speed applications for separation control on aircraft wings.[18] However, applied parametric studies of airfoils equipped with VGs are uncommon. Fouatih et al[20] recently conducted a parametric study on a slender 15%-thick NACA4415 airfoil with delta vane devices at a chord-based Reynolds number $\mathrm{Re}_c = 2 \times 10^5$. The authors observed low sensitivity to the VG packing density (*d* and *D*). Optimum vane angles (in terms of maximum C_l/C_d) were in the range of $\pm 11 - 12^\circ$ for rectangular and delta vanes. Gao et al[21] performed computational fluid dynamic simulations on the DU97-W-300 airfoil at $\mathrm{Re}_c = 3 \times 10^6$ with different VG vane lengths, spacing, and height, albeit with a rather limited parameter space. The authors hint that stronger vortices do not necessarily benefit flow controllability. Furthermore, an increase in vane length from 2.8*h* to 3.4*h* was detrimental to performance, whilst increasing vane height from 5 to 6 mm increased lift and $C_l|_{\max}$, at the cost of higher drag and reduced airfoil efficiency.

1.2 | Motivation and present work

The complex flow phenomena associated with VGs have hampered the robustness and effectiveness of engineering models. Numerical tools will

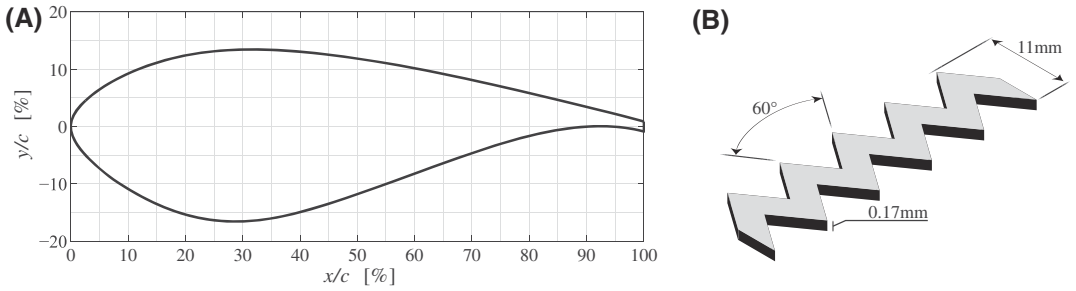

FIGURE 2 A, DU97-W-300 model profile; B, ZigZag tape geometry

therefore play an important role in the continued development of VGs for flow separation control, but better means of validation for thick wind energy airfoils are necessary. This paper aims to bridge this gap by tackling the following research questions:

1. What is the performance sensitivity of a thick airfoil section to different VG designs?
2. What is the relative importance of the VG design parameters?
3. How are loading dynamics altered in the presence of VGs?

To this end, the present work studies the effect of various passive vane–type VGs on the performance of the DU97-W-300 airfoil at $\mathrm{Re}_c = 2\times10^6$, in clean and rough conditions. This airfoil, shown in Figure 2, was designed and tested by Timmer et al[22] for inboard wind turbine blade sections. The approach, including VG design and experimental procedure, is discussed in Section 2. Oil-flow visualizations (OFV) and polars are presented in Section 3 and Appendix A. Section 4 presents a discussion of the unsteady loading characteristics, and conclusions follow in Section 5.

2 | APPROACH

2.1 | Airfoil model and wind tunnel facility

The DU97-W-300 airfoil was tested in the closed loop, low turbulence tunnel at Delft University of Technology. The test section is octagonal, measuring 1.80 m × 1.25 m and 2.60 m long. The model had a chord $c = 0.65$ m, a thick trailing edge of 1.7% chord and spanned the height of the test section, giving an aspect ratio of approximately 1.92. A traversable wake rake for assessing the total drag was positioned approximately 60%c downstream the airfoil trailing edge. All polars were acquired at $\mathrm{Re}_c = 2\times10^6$ (Mach number 0.13), for which the tunnel turbulence levels were below 0.1%. Model blockage in the test section was around 10% near $C_l|_{\max}$ for the uncontrolled airfoil. Polars were acquired in the freely transitional regime, as well as in forced transition. The latter was enforced using ZigZag (ZZ) tape on the airfoil upper surface along the entire wing span. The thickness of this strip was 0.17 mm, with a width of 11 mm, its leading edge fixed at 5% from the airfoil leading edge on the upper surface. The uncontrolled airfoil polars are given in Figure 3 and compared with viscous-inviscid simulations performed in RFOIL.[23] Transitional simulations with the e^N method [24] were produced using a critical amplification factor $N = 11$. Rough calculations initiate a turbulent boundary layer on the suction side at the location of the ZZ tape. Note also the consistency between the present clean performance and the original liquid manometer measurements of Timmer et al.[22] Throughout the paper, "clean" and "tripped/rough" pertain to the state of the boundary layer. The presence of the VGs is described as a "controlled" case; "NoVG" refers to the uncontrolled airfoil.

2.2 | Instrumentation and data acquisition

The normal and tangential airfoil loads (C_n and C_t) were determined through the model and wake rake pressure measurements, acquired through a DTC INITIUM data acquisition system. A total of 102 surface pressure taps surrounded the airfoil model, including one in the midsection of the blunt trailing edge. The wake rake was fitted with 67 total pressure and 16 static pressure tubes. The lift was evaluated according to

$$C_l = C_n/\cos\alpha - C_d\tan\alpha, \tag{1}$$

where C_d was determined from the wake rake or model pressure drag. The final lift and drag coefficients were obtained after modification through wind tunnel corrections for model and wake blockage, and streamline curvature.

The spanwise uniformity of the uncontrolled flow was assessed with wake rake traverses at different angles of attack. One such pass is shown in Figure 4A for $\alpha = 6.2°$. In the attached regime, the flow is sufficiently uniform. On the other hand, VGs induce a 3-dimensional flow, but when arranged in a uniform array, the flow becomes spanwise periodic. To assess the airfoil drag with VGs from the wake rake, a spanwise traverse was conducted for each angle of attack at 1.2mm/s and spanning a range of three VG pair spacings ($3 \times D$). The resulting spanwise-averaged value, C_d, was then considered as the representative drag. A typical wake scan is shown in Figure 4A at 3 angles of attack. At higher angles of attack, and thus stronger APGs, the vortices will tend to diffuse more and thus leave a weaker signature.[25] The peaks correspond to the upwash regions. Here,

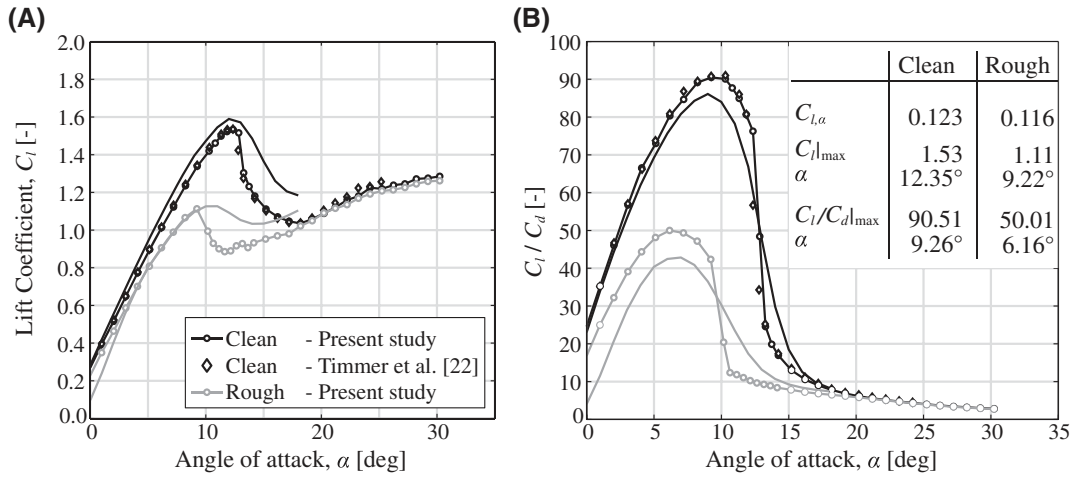

FIGURE 3 A, Lift polar and B, aerodynamic efficiency for clean and rough conditions. Symbols and tabulated data represent measurements, plain lines RFOIL predictions

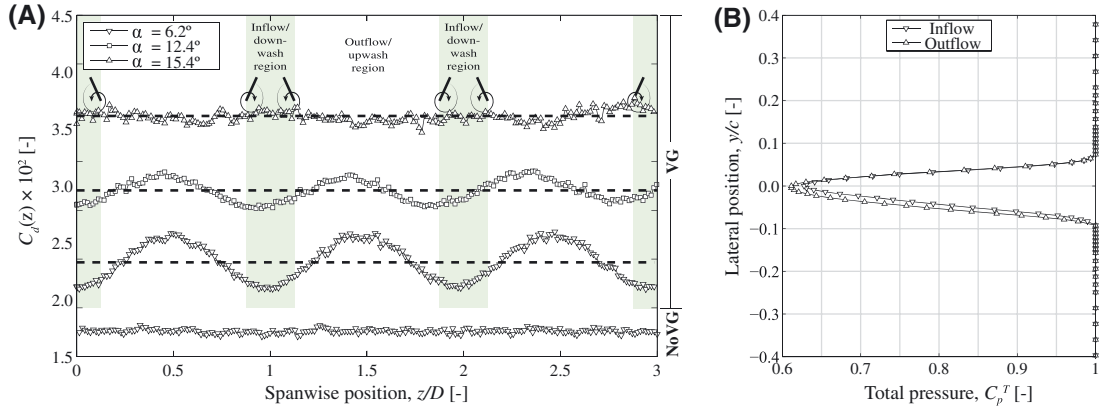

FIGURE 4 A, A typical drag signal along a wake rake traverse; dashed lines indicate the spanwise-averaged value; case: uncontrolled and vortex generator (VG) base design in free transition; B, total pressure profile in the airfoil wake sampled at $\alpha = 12.4°$ at an inflow and outflow position along the span; $y/c < 0$ corresponds roughly to the wake emanating from the suction side of the airfoil. case: VG base design in free transition [Colour figure can be viewed at wileyonlinelibrary.com]

adjacent (CU) vortices eject low momentum boundary layer fluid that manifests downstream as a stronger wake deficit. This is further illustrated by the wake profiles of Figure 4B, sampled at an outflow and inflow position (peaks and troughs of Figure 4A). Notice how the wake profile variations largely materialize from the suction side, where the VGs are located.

For uncontrolled cases, pressures for each angle of attack were sampled for 10 seconds before $C_l|_{max}$, and 30 seconds in the stall regime. With VGs, the total sampling time ranged from 45 to 90 seconds (determined by the duration of the wake rake traverse). Beyond $C_l|_{max}$, the wake rake was not operated because of the extent and unsteadiness of the separating wake. The drag in this operating regime was instead assessed from the model pressures, giving only the pressure drag component, and the sampling time was fixed at 30 seconds. In all cases, the pressures were sampled at approximately 337 Hz. The airfoil boundary layer was measured for the uncontrolled flow via the same data acquisition system and using a small traversable total pressure probe with a nozzle of 0.5 mm. The complete setup is shown in Figure 5, showing the telescopic aid for positioning the probe.

The transition location was assessed using a handheld stethoscope and shown for 2 Reynolds numbers in Figure 6. Graduations spaced 5%c on the model increased the precision of the measurements. The results compare fairly well with the expectations, particularly in the linear $C_l - \alpha$ range. This device was also used to ensure transition behind the ZZ strip; in all cases, transition to turbulence appeared complete within one strip's width downstream of its trailing edge.

Oil-flow visualizations were conducted by first coating the model with a solution of liquid paraffin and fluorescent dye. The model was then illuminated with ultraviolet light and a Nikon DSLR camera used to acquire the images. Spanwise rules equispaced 10% chord were marked to facilitate image analysis.

2.2.1 | Experimental error sources and uncertainty

Signal drift occurs because of variations of atmospheric temperature and pressure, as well as heating up of electronic components. This is accounted for by rebiassing the pressure levels before every new run. The resolution of the electronic pressure scanners ranged from 0.2 to 2.0 Pa. Uncertainty

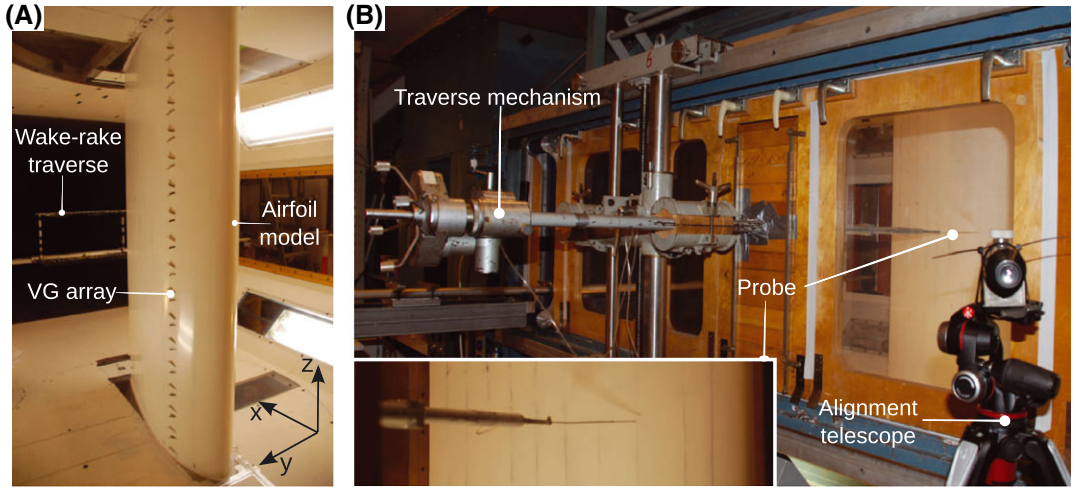

FIGURE 5 A, Typical test-section setup showing the wake rake aft of the wing section; B, boundary layer measurement setup. VG, vortex generator [Colour figure can be viewed at wileyonlinelibrary.com]

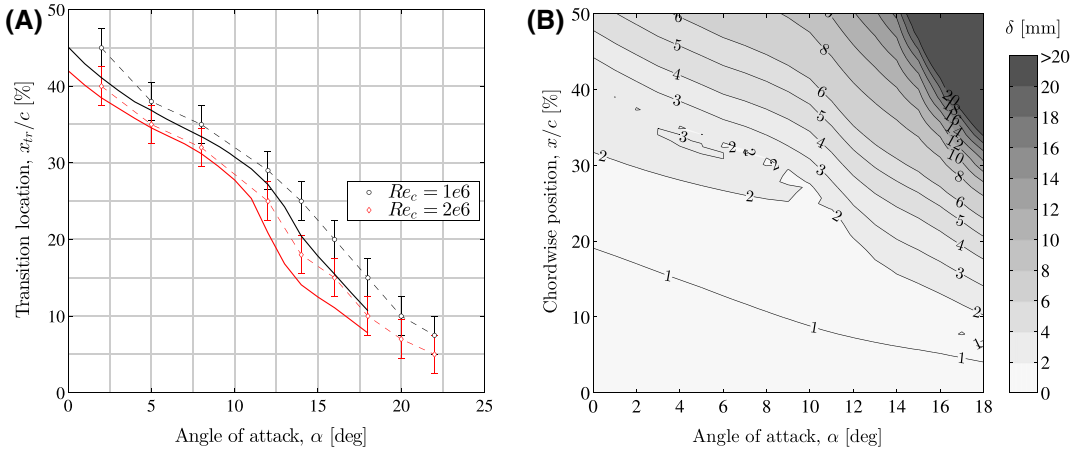

FIGURE 6 A, Transition location on the airfoil suction side at 2 Reynolds numbers. Symbols/dashed lines indicate measurements, and solid lines represent RFOIL predictions; B, boundary layer thickness estimates in $(\alpha, x/c)$ space at $\mathrm{Re}_c = 2 \times 10^6$ for natural transition [Colour figure can be viewed at wileyonlinelibrary.com]

in the angle of attack was below 0.01°. Sampling errors were at least an order of magnitude lower due to the large sample size for each data point. The final uncertainty propagation results in a worst-case error of 1% for C_p, 0.1% on C_l and 2% on C_d. The boundary layer probe traverse could resolve 0.01 mm, but the uncertainty of the absolute wall position is approximately ±0.25 mm. The absolute lift and drag quantities in the stalled regime are less reliable because of unsteady, 3-dimensional flow separation.

The periodic placement of VGs gives rise to spanwise-periodic flow and loading. For the wake rake drag, the periodicity is addressed by spanwise-averaging the wake traverses along the VG array. In contrast, the true spanwise-averaged lift is not possible from the measurements due to the staggering of the pressure taps; however, computations showed that vortex-induced disturbances are localized around the vanes, and the net effect on the measurements is negligible.[26] Pressure signals disrupted by the VG strips and ZZ tape were replaced by interpolated estimates from adjacent undisturbed signals, whilst the small size (<0.4 mm) and staggered formation of the pressure taps minimized their mutual interference.

2.3 | Vortex generators

This section first presents the VG base design and its variants. Dimensions are initially defined parametrically in terms of the vane height *h*. A final design is then presented in section 2.3.2, where the physical dimensions of *h* are determined based on operational considerations.

2.3.1 | Base design and test configurations

The salient VG parameters, summarized in Figure 1A, pertain to the (1) vane geometry and (2) array configuration. Based on the reviewed literature, the following robust base design for separation control was defined:

a. $h/c \approx 1\%, L = 3h, \beta = \pm 15°$, delta wing planform (referred henceforth as simply delta) at $x/c = 20\%$, measured between the airfoil and VG strip leading edges.

b. $d = 3.5h, D = 7h$, CtR, CD.

Design variants were then obtained by modifying these parameters relative to the base design. Three vane heights were investigated, with an additional smaller ($h/c < 1\%$) and larger ($h/c > 1\%$) variant. These were in-turn tested at different chordwise positions, $10\% < x/c < 50\%$, within clean and rough conditions. The remaining variants were only measured in a clean boundary layer at $x/c = 20\%$, with vane angles $10^\circ < \beta < 25^\circ$ and vane lengths $2h < L < 5h$. A CDA variation was designed such that $b = 0.2L$ (see Figure 1A), resulting in a 20% increase of the vane planform. The configuration was also varied with a larger spacing $D = 10h$, and ensuing CoR and CtR CU variants. The complete parameter space is summarized in Table 1.

2.3.2 | Sizing the vane heights

The independent parameter h was required to dimension the self-similar designs. To determine a range of sensible values for the VG vane heights, it was first necessary to understand the uncontrolled flow. For a given operating point in the post-stall region, the VGs would only work if mounted in front of the mean separation line. At this position, h/δ must be large enough to generate sufficient streamwise vorticity to prevent separation. However, placing the VGs too far forward would incur increasing parasitic drag at lower angles of attack. This is especially true if the array is ahead of the natural laminar-turbulent transition location x_{tr}. Thus, both the boundary layer thickness as well as x_{tr} were required for sizing the VGs.

Measured and predicted transition locations are compared in Figure 6A. Increasing the Reynolds number moves x_{tr} forward for a given pressure gradient (ie, α). The trend also implies that the more forward the VG mounting location, the larger the additional drag due to the forced turbulent boundary layer. RFOIL is formulated in terms of integral parameters such as the displacement and momentum thickness (δ^* and θ). Therefore, the physical depth of the boundary layer may be estimated as

$$\delta = \begin{cases} 2.9\delta^* & \text{for } x < x_{tr} \quad \text{(laminar)} \\ \theta\left(3.15 + \frac{1.72}{H-1}\right) + \delta^* & \text{for } x > x_{tr} \quad \text{(turbulent)} \end{cases}, \tag{2}$$

TABLE 1 Overall dimensions of the VG sets in the parameter study[a]

Shape/Config.	Transition	x_{VG}/c [%]	h [mm]	β [deg]	d/h [–]	D/h [–]	L/h [–]	d [mm]	D [mm]	L [mm]
Delta/CtR CD	**Free**	**20**	**5**	**±15**	**3.5**	**7**	**3**	**17.5**	**35**	**15**
Delta/CtR CD	Free/Forced	10:10:40	2.5	±15	3.5	7	3	8.75	17.5	7.5
	Free/Forced	10:10:50	5	±15	3.5	7	3	17.5	35	15
	Free/Forced	20:10:50	10	±15	3.5	7	3	35	70	30
	Free	20	5	±10, ±12, ±18, ±20, ±25	3.5	7	3	17.5	35	15
	Free	20	5	± 15	3.5	7	2, 4, 5	17.5	35	10, 20, 25
	Free	20	5	± 15	3.5	10	3	17.5	50	15
Cropped-Delta/ CtR CD	Free	20	5	± 15	3.5	7	3	17.5	35	15 ($b = 3$ mm)
Delta/CtR CU	Free	20	5	∓ 15	3.5	7	3	17.5	35	15
Delta/CoR	Free	20	5	15	–	7	3	–	35	15

Abbreviations: CD, common downwash; CoR, corotating; CtR, counter-rotating; VG, vortex generator.

[a]Base design described in first row (bold).

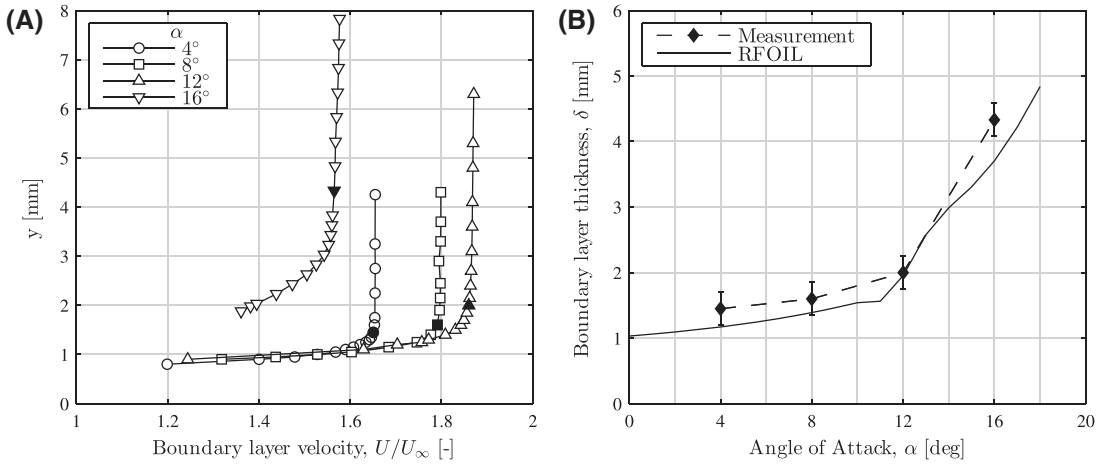

FIGURE 7 A. Measured boundary layer profiles at $x/c = 20\%$. Filled black symbols indicate boundary layer edge; B, boundary layer thickness evolution with angle of attack. Case: clean, uncontrolled airfoil

where the shape factor $H = \delta^*/\theta$. Blasius flat-plate relation was used for laminar flow,[27] whereas the incompressible entrainment coefficient is used in the case of turbulent flow.[28] For a range of chordwise positions and angles of attack, δ is shown in Figure 6B. Based on these calculations, the original design specification and manufacturing constraints, VG heights of 2.5, 5, and 10 mm were chosen, corresponding to $h/c \approx 0.4\%, 0.8\%, 1.6\%$.

The boundary layer measurements provided some design verification for the actual h/δ. Using the total pressure measured in the boundary layer and the model static pressure at $x/c = 20\%$, the velocity profile U can be estimated as shown in Figure 7A. The boundary layer edge was set at the point, where the spanwise vorticity ($\approx |-\partial U/\partial y|$) drops below 1% of its maximum and shown in Figure 7B. The rapid evolution of δ after $\alpha = 12^\circ$ indicates a decambering effect due to flow separation, and at $\alpha = 16^\circ$, $\delta \approx 4.5$ mm. Therefore, the reference boundary layer thickness was arbitrarily defined for $(\alpha, x/c) = (12^\circ, 20\%)$, where $\delta \approx 2$ mm. This reference condition represents the maximum lift angle for the clean uncontrolled airfoil, at a position residing ahead of the small trailing edge separation zone, giving $h/\delta \approx 1.25 \pm 0.03, 2.50 \pm 0.06$, and 5.00 ± 0.12. Note that VG cases operating in rough conditions will experience a slightly thicker boundary layer, lowering these reference values slightly.

2.3.3 | VG construction and mounting

The VG profiles were individually formed and attached to mounting strips (MS), spanning the length of the wing. This eased the interchanging of arrays during the tests. The vanes and MS were manufactured from 0.2-mm spring steel, and the material thickness was accounted for when designing the VG heights. The strips were attached with double-sided adhesive tape according to predesigned templates corresponding to the specific array design. The VG arrays were mounted in such a way to direct fluid into (downwash) the wing-wall junction where possible to alleviate the influence of corner separation.

3 | RESULTS

3.1 | Oil-flow visualization

The effect of the VGs is qualitatively assessed through the response of an oil film on the airfoil surface. In Figure 8, the suction side of the airfoil is visualized at three increasing angles of attack. The flow direction in these images is from right to left. Before $\alpha = 15^\circ$, the flow is attached in the uncontrolled case. The bright band running along the span around the 30% c to 40% c location is the laminar separation bubble. It is evident that this moves forward with increasing α. Comparing the location of the separation bubbles and the strip leading edge at $\alpha = 0^\circ$ and 8°, the VGs evidently

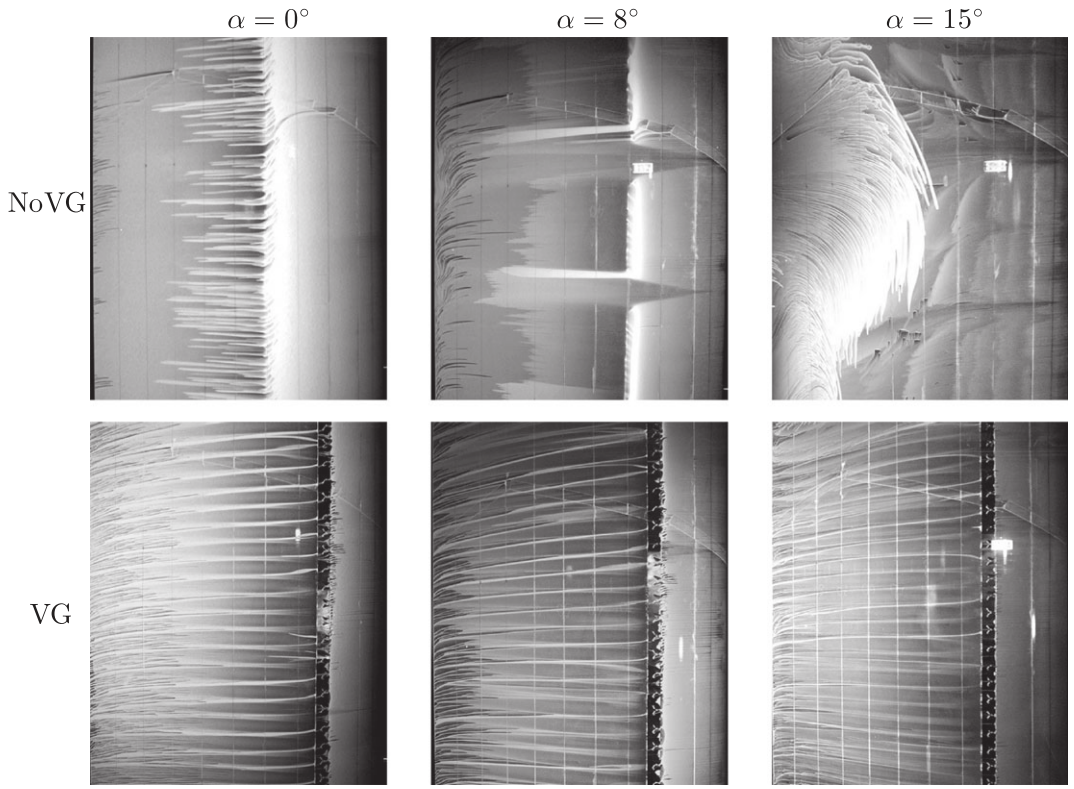

FIGURE 8 Oil-flow visualization of the clean airfoil suction side for increasing angle of attack. Case: without and with (base design) vortex generators. Flow direction: right to left. NoVG, uncontrolled airfoil; VG, vortex generator

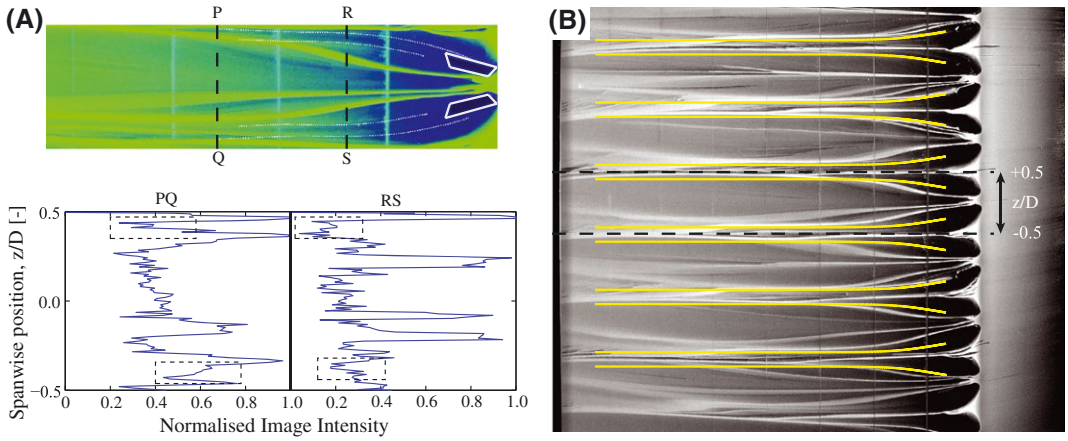

FIGURE 9 A, Detailed oil-flow visualization over a spanwise period (top) with complimentary image analysis for vortex signature detection (bottom); B, visualization overlayed with predicted vortex paths (yellow dashed lines) in the streamwise-spanwise plane (Equations 3-4). Case: h =10 mm, $x_{VG}/c = 20\%$, airfoil suction side, $\alpha = 0^\circ$ in free transition [Colour figure can be viewed at wileyonlinelibrary.com]

induce additional drag by forcing earlier transition at low angles of attack. However, the separated suction side flow is completely reattached with VGs at $\alpha = 15^\circ$. The structure of the separated flow is typical of mounted wings in wind tunnels, consisting of stall cells over the planform and corner cells at the wing-wall junction.[9]

Distinctly aligned oil streaks are observed behind the VGs, indicative of the vortex passages. However, some considerations of the vortex flow field offer a more detailed interpretation (see Figure 9). The region directly between the vortex and the surface is highly sheared and should result in a local oil deficiency. Further away from the vortex, as the induced secondary flow field diminishes, the oil film gradually adheres better to the surface. The passage of the vortex should therefore be characterized by a dark band flanked by brighter regions where oil has been redeposited. This is evidenced in Figure 9A, where the dark band lies between the 2 sets of dotted lines. The image intensity is sampled along 2 lines "PQ" and "RS" over a spanwise period $-0.5 < z/D < 0.5$. The vortex signature can be deduced from the preceding arguments, indicated by corresponding rectangular contours. This interpretation is aligned with the observations of Holden and Babinsky[29] for surface flow characterization behind wedge and vane type VGs.

Furthermore, quantitative information may be obtained by considering the inviscid vortex trajectories predicted from Jones vortex model.[10] The equations for these trajectories (in x, y, and z coordinates) are given as

$$\mathrm{cosec}^2(kz) + \mathrm{cosech}^2(ky) = C. \tag{3}$$

$$x = \frac{1}{k\gamma}\int_{(kz)_1}^{(kz)_2}\left[1 + \frac{\tanh^2(ky)}{\tan^2(kz)}\right]\sinh(2ky)\,\mathrm{d}(kz). \tag{4}$$

where k is $\frac{2\pi}{D}$, the wavenumber of the array; C is an integration constant; and γ is a nondimensional vortex strength. The model is initialized with vortex positions corresponding to the tips of the VG vanes. Focussing on the near wake region (up to 10h behind the VGs) in which the trajectory displays the highest curvature, the vortex strength parameter was tuned to give the best match with observations considering the centre dark band as the true vortex passage. The resulting trajectories were superposed on the oil film image in Figure 9B.

Incidentally, this procedure demonstrates an inverse method for estimating the initial vortex strength. This was explored further by analysing the near wake images from the VG base design in Figure 10. As before, the vortex strength parameter was manually tuned to obtain a best overlay with the dark band, thus obtaining $\Gamma = f(\alpha)$. We next consider $\Gamma = \kappa \cdot hU_{VG}$ to be the generalized functional form of the vortex strength, where κ is a function of the device geometry and configuration.[14,16] This relation will be used to benchmark the method.

Airfoil surface pressure measurements were then used to deduce the local velocity U_e outside the boundary layer, whose sensitivity to α is shown at the chordwise position of the VG tip ($\approx 23\%\,c$) in Figure 11A. Since the base design vanes exceed the boundary layer thickness at $\alpha = 16^\circ$, it is reasonable to use U_e as an approximation for the VG tip speed, U_{VG}. The resulting trend between Γ and hU_e is linear, as shown in Figure 11B, with $\kappa = 1.8$. For a similar VG arrangement in a flat-plate boundary layer, Lögdberg et al[14] directly measured the vortex strength and reported $1.2 < \kappa < 2.0$, depending on the definition of the total circulation. The estimated Γ is therefore not only in the correct order of magnitude but also appears to be a reasonable approximation.

Limiting the analysis to the near wake region reduces the method uncertainty in 2 respects. The high trajectory curvature in the near wake is most sensitive to changes in Γ and thus best suited for the calibration procedure. Additionally, for this setup, the oil traces dip downwards under the influence of gravity. Particularly at higher angles of attack, this effect may skew the observations, as reflected in the growing error bars in Figure 11B. These uncertainty bounds indicate the edge-to-edge extremes of the fitted paths across the dark band in the near wake.

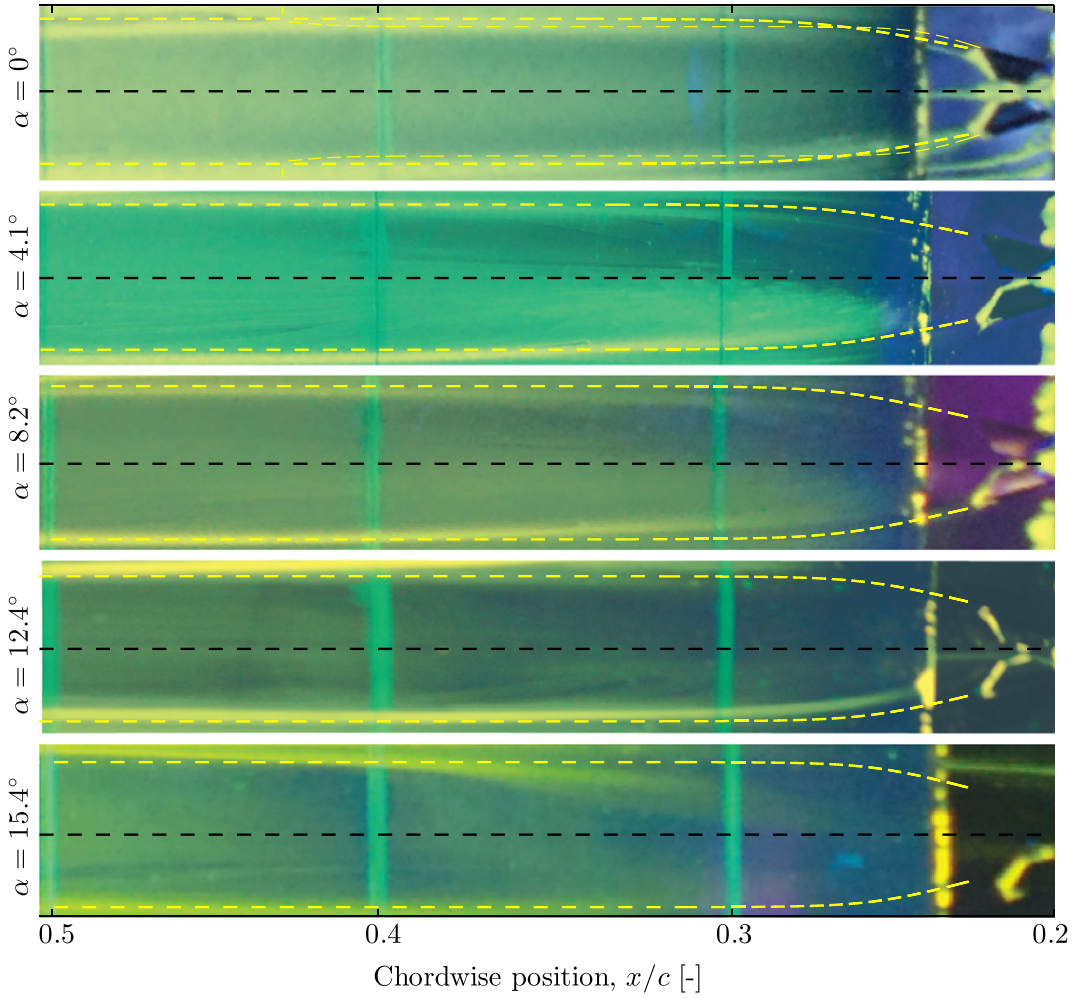

FIGURE 10 Base design near wake oil-flow visualisations for increasing angles of attack. Flow direction: right to left [Colour figure can be viewed at wileyonlinelibrary.com]

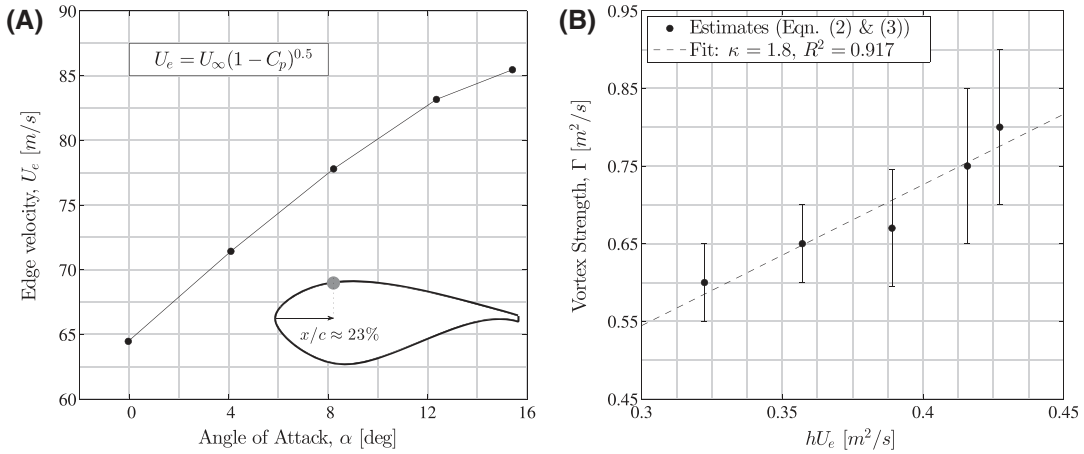

FIGURE 11 A, Deduced edge velocity; B, circulation estimates for the vortex generator base design (R, coefficient of determination). $U_\infty \approx 45$ m/s

3.2 | Performance polars

In the following sections, reference is made to 2 types of figures. Lift and drag polars for the different VG cases have been compiled in Appendix A. Secondly, airfoil performance metrics are compared in Figures 14 and 16, namely,

- the maximum lift coefficient and its corresponding angle of attack ($C_l|_{max}$, α_{CLM}),
- the drag at $\alpha = 0$ ($C_d|_{\alpha=0°}$),

- the lift slope ($C_{l,\alpha}$), and
- the aerodynamic efficiency ($C_l/C_d|_{\max}$) at its corresponding angle of attack.

Note that the first local maximum C_l attained is considered the maximum lift, and $C_{l,\alpha}$ is evaluated over $\alpha = [0^\circ, 4^\circ]$.

3.2.1 | Influence of the MS

The MS method used in this experiment is commonly used in practice to facilitate the attachment process. If the MS height exceeds the critical roughness height, transition is forced at its leading edge, degrading performance. In addition, failure to account for the strip in numerical models may cause discrepancies with measurements.[30] To investigate this, the 10-mm VGs were separately tested by mounting the vanes directly to the model at $x/c = 20\%$. In Figure 12, the sharp transition at the strip is clearly distinguished from the oncoming laminar layer—the higher shearing of the turbulent boundary layer behind the strip tends to tear oil away from the surface and thus does not appear as bright when illuminated. Without the strip (Figure 12B), small regions in between the vanes have a higher concentration of oil followed by a sharp transition. This indicates the persistence of a laminar boundary layer in between the vanes and thus results in slightly lower skin-frictional drag. The sharp boundary between the laminar inflow wedges, and the VG wake region is likely due to the horseshoe vortex emanating from the vane-wall junction,[29,31] as detailed in an OFV of a single vane in Figure 12C.

Additionally, the MS forces a local stepwise increase in the boundary layer thickness. This gradually grows downstream and effectively de-cambers the airfoil, reducing lift and causing earlier turbulent separation. The extent to which this affects performance is quite remarkable, as shown from the polars of Figure 13. A steady increase of 1 drag count ($\approx 5-6\%$) with the MS is noted in the linear $C_l - \alpha$ range, accompanied by a reduction in $C_l|_{\max}$ and the glide slope.

3.2.2 | Influence of VG vane geometry and chordwise placement

Section 2.3.2 showed how the choice of the vane height and array chordwise position are coupled through the evolving boundary layer thickness δ. The result of these variations is shown in Figure A1. The trends shown in Figure 14 indicate an increasing $C_l|_{\max}$ until $x_{VG}/c = 30\%$, with a decrease in the corresponding angle of attack, for all VG heights. The lift polars also show that the more rearward the mounting position, the more abrupt the stall characteristic. The largest VG ($h = 10$ mm) only attains higher lift after the 30%c position. In general, it may also be noted that the larger the VG, the more abrupt the stalling characteristics. Higher drag is observed at $\alpha = 0^\circ$ and tends to reduce the further aft the mounting position. This

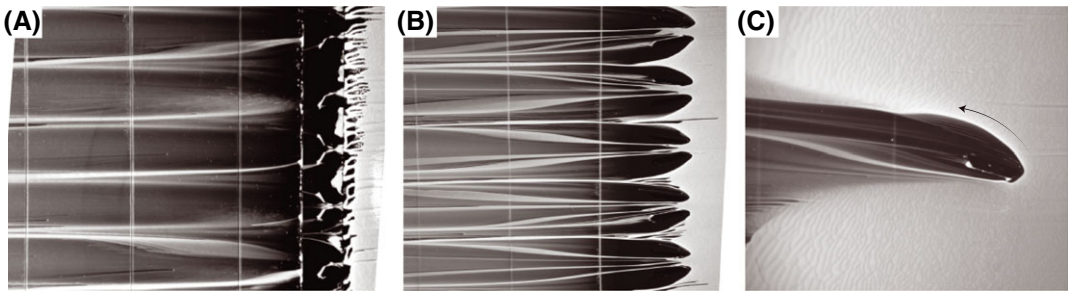

FIGURE 12 Flow visualization of a VG array, A, with and B, without a mounting strip; C, the flow past a single vane, detailing the passage of the horseshoe vortex. Case: $h = 10$ mm, $x_{VG} = 20\%c$, airfoil suction side, $\alpha = 0^\circ$ in free transition. Flow direction: right to left [Colour figure can be viewed at wileyonlinelibrary.com]

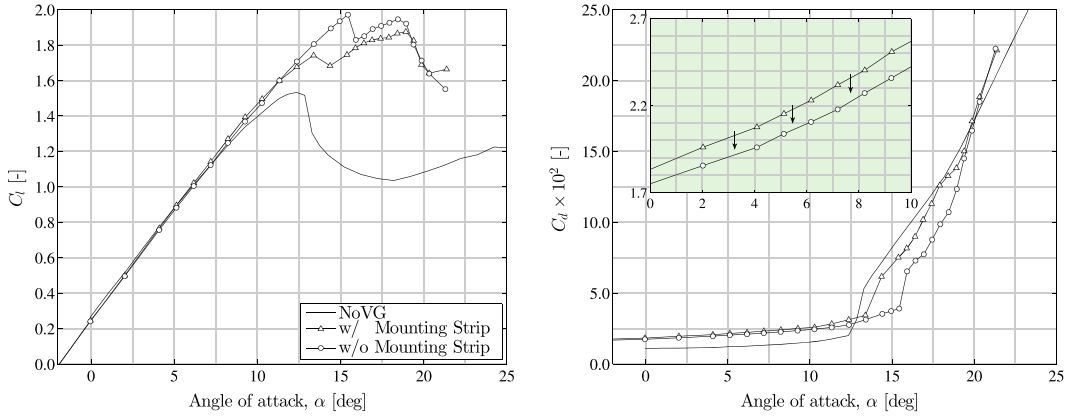

FIGURE 13 Lift and drag polar showing the influence of the vortex generator mounting strip. NoVG, uncontrolled airfoil [Colour figure can be viewed at wileyonlinelibrary.com]

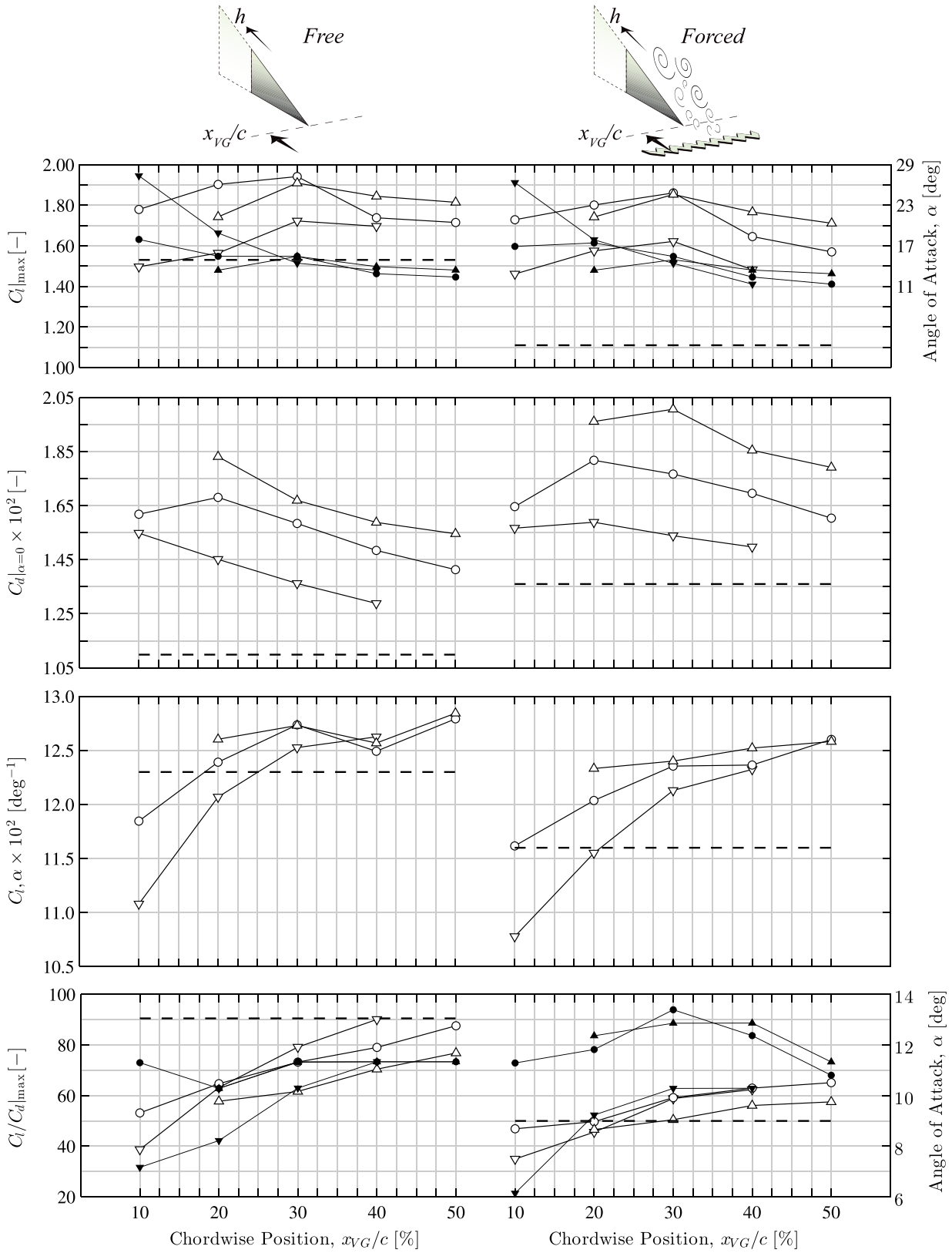

FIGURE 14 Metrics summarizing the effect of chordwise array placement, vane height, and boundary layer state. Symbols: $h = 2.5$ mm (▽); $h = 5$ mm (○); $h = 10$ mm (△). Filled white symbols represent the metric (left ordinate), and filled black symbols show the corresponding angle of attack, when applicable (right ordinate). Dashed lines indicate metrics (left ordinate) for the uncontrolled case. The top-most schematics illustrate the varied parameters relevant in each column [Colour figure can be viewed at wileyonlinelibrary.com]

is to be expected of larger VGs because of the larger frontal area and "spoiler"-type drag. The maximum efficiency is attained with the smallest VGs after the 20%c location. Meanwhile, the 10-mm VGs are consistently less efficient than the 5 mm, over the whole chordwise range tested. The angle of attack at $C_l/C_d|_{\max}$ gradually increases downstream for the 2.5 mm but remains mostly constant for the 5 and 10 mm. The 2.5-mm VGs reduce

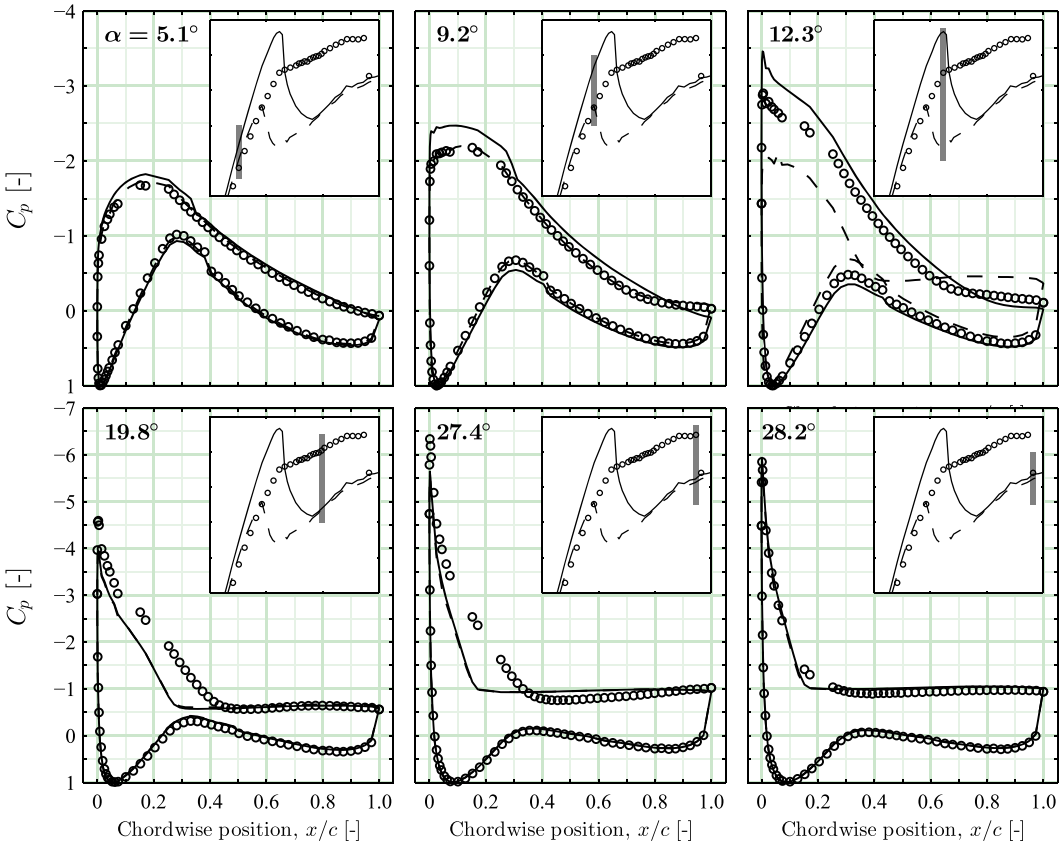

FIGURE 15 Pressure distributions for increasing angles of attack, sampled along the lift polar as indicated in the inserts; clean (-) and rough (- -) uncontrolled cases; 2.5-mm VGs at $x/c = 10\%$ in clean condition (∘) [Colour figure can be viewed at wileyonlinelibrary.com]

$C_{l,\alpha}$ relative to the uncontrolled airfoil when mounted before the 30% c location. This also occurred for the 5-mm VGs at $x/c = 10\%$, partly owing to the disruption of laminar flow. In all cases, $C_l/C_d|_{\max}$ is consistently lower compared with the uncontrolled, clean airfoil.

These design variations were also investigated with an artificially roughened boundary layer using the ZZ tape. The plots are shown in Figure A2 with corresponding metrics in the right panel of Figure 14. Relative to the uncontrolled, rough conditions, the performance with VGs is generally improved and only the 2.5-mm VGs at $x/c = 10\%$ result in a noticeable slope reduction. Generally speaking, the improvement in maximum lift relative to the uncontrolled condition is noticeably higher in the rough cases, and $C_l/C_d|_{\max}$ is also improved for all cases mounted at $x_{VG}/c > 20\%$. In the attached regime, the presence of roughness increases (offsets) the airfoil drag in a similar manner as observed for the MS. For the 10-mm VGs, this roughness-induced drag offset is approximately 10% to 20%. Thus, boundary layer thickening due to leading edge roughness is expected to reduce the relative impact of the MS. The presence of roughness on the controlled airfoil then effectively results in a slight loss of performance, compared with the clean-controlled scenarios.

Closer inspection of the 2.5-mm VG lift polar at $x/c = 10\%$ reveals 2 distinctive regions characterized by different slopes. This is particularly evident in the clean condition. In the first region until $\alpha = 12.35°$, it is conceivable that the drag penalty of the small VGs outweighs any gains from delayed separation. This results in the decambering effect evident from Figures A1 and A2 and is similar to the effect of the ZZ tape on the uncontrolled airfoil performance. This similarity is explored in the first 2 panels of Figure 15 by comparing pressure distributions for the clean and rough uncontrolled performance with that of the 2.5-mm VGs (in clean condition). Beyond $\alpha = 12.35°$, the lift slope drops abruptly as a result of encroaching trailing edge separation, as evidenced in the remaining panels of Figure 15. However, generating the vortices at 10% chord allows more range for their development, which means they remain effective at the higher attitudes. Thus, the initial performance detriment owing to the VG disturbance is compensated somewhat at higher attitudes.

The effect of the vane angle is illustrated in Figure A3A. The trends, now shown in Figure 16, show a clear optimum at ±12°, yielding a $C_l|_{\max}$ of 2.03 at $\alpha = 18°$. A subsequent increase in vane angle yielded lower maximum lift, largely occurring around $\alpha = 15.5°$. The drag steadily rises as β increases, as seen from the drag polar, and summarized in the metric chart. The lift slope remains rather constant for all variations, but $C_l/C_d|_{\max}$ decreases steadily with increasing β. The results show that small changes in the vane angle have a noticeable impact on the performance; a small 2° increment from $\beta = \pm 10°$ to 12° reduces $C_l/C_d|_{\max}$ by 5% but increases $C_l|_{\max}$ by 10%. Experimental evidence has previously revealed a linear relation between vortex strength Γ and the vane angle, generally speaking for angles below 20°, but the relationship between Γ and airfoil lift does not follow the same trend.[12,15,32] In fact, the metric chart shows an overall inverse relationship between $C_l|_{\max}$ (and $C_{l,\alpha}$) and β. The higher device angles pose more spoiler drag, and the stronger vortex also induces more drag (in the form of rotational losses and higher skin friction). Additionally,

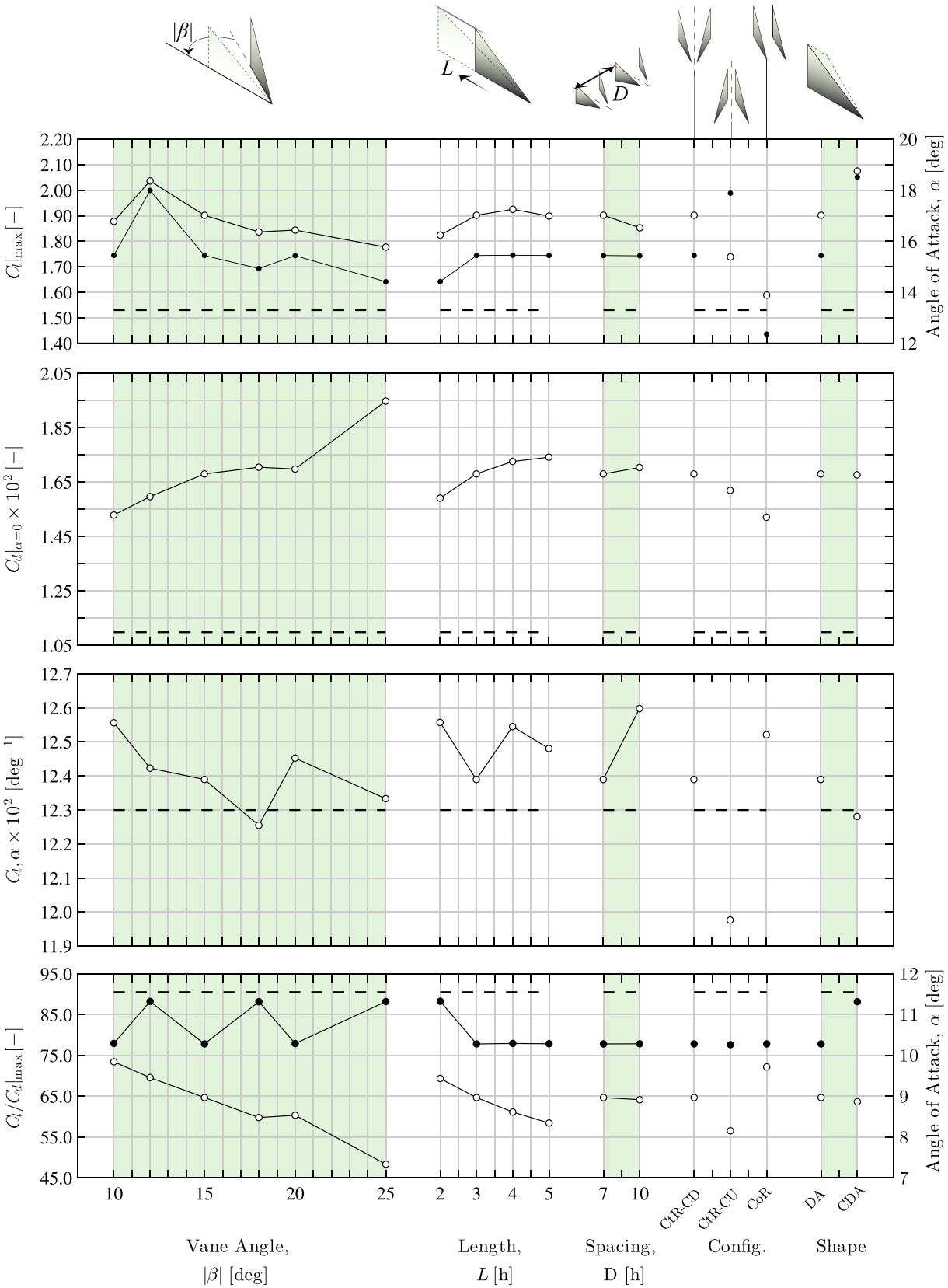

FIGURE 16 Same as Figure 14 for the vane angle and length, array spacing and configuration, and vane shape [Colour figure can be viewed at wileyonlinelibrary.com]

the quality of the vortex may degrade at higher angles because of local separation on the vane itself.[11] However, this would require localized flow field measurements for further verification.

With β fixed at $\pm 15^\circ$, the vane length is varied from 2 to 5h, the effect of which is shown in Figure A3B. The $L = 4h$ design delivers the highest lift. Higher drag is induced as the vanes are lengthened and hence $C_l/C_d|_{\max}$ also decreases. As with the vane angle, $C_l|_{\max}$ displays a complex relationship with L/h.

The CDA variation is additionally benchmarked against the baseline Delta vanes in Figure A3C. $C_l|_{\max}$ increased by approximately 10%, with only a marginal decrease in $C_l/C_d|_{\max}$. This occurs with only a slight reduction in the lift slope, meaning that the CDA variation performs better, essentially extending the lift polar.

In this section, we have seen examples of linear behaviour, such as the monotonic variation of $C_l|_{\max}$ and α_{CLM} in ($h = 10$ mm, x_{VG}/c) space. This implies that the change of parameters primarily results in an extension of the lift polar along some representative averaged curve. However, in most cases, the results suggest nonlinear relationships, contrary to numerical predictions[33] or the linearized simplifications of engineering models. [1,11]

3.2.3 | Influence of VG array configuration

The relative orientation of the vanes is investigated with 2 typical variations: a CtR CU and CoR configuration. These sensitivities are shown in Figure A3D. Both variations result in a deterioration of maximum lift. The CU configuration is outperformed by the base design, in terms of both $C_l|_{\max}$ and $C_l/C_d|_{\max}$, as vortices are immediately convected away from the surface. The CoR array is obtained by removing like-signed vanes from the base design, thus producing half the circulation per unit span compared with the baseline. The drag is therefore lower for this configuration at low α, but the control ability of this design variation is severely reduced. According to Pearcey,[11] CoR arrays ought to be effective as long as their initial spacing exceeds 3h. However, Godard and Stanislas[19] observed half the increase in skin friction from a CoR array, compared with a CtR array with the same geometry, indicating a lower efficiency of the CoR array. Additionally, an infinite system of CoR wall-bounded vortices of equal strength will drift laterally by up to 15° relative to the streamwise direction.[11] Therefore, a rough estimate indicates that up to 3% of the airfoil planform behind the VGs may become devoid of vortex action. Further, the effectiveness of an entire (finite) CoR array may be dictated by reduced control authority at the edges because of vortex ejection, and it is precisely the wing-wall junction, near the array edge that is most likely to separate first. The result therefore demonstrates that failure to control pockets of separated flow clearly has an effect on the global wing performance. Thus, given the complex flow separation behaviour on a turbine blade, the observations are equally relevant for practical applications.

The effect of increasing the interpair spacing is shown in the polars of Figures A3E. A slight reduction in maximum lift is observed for $D = 10h$, which is preceded by a decreased lift slope, as might be expected due to the lower circulation per unit span of approximately 30%. The drag at low angles of attack is approximately 2.9% to 2.2% higher in the range $\alpha = 0^\circ$ to 10° for the larger spacing, despite the reduction of Γ/D. However, the larger spacing means that vortices originating from a CD pair commence farther from adjacent pairs. The vortex traces in Figure 9B support Jones'[10] and Pearcey's[11] theoretical demonstrations that CtR (equal strength) vortex arrays gradually reorganize to form CU pairs. The larger spanwise spacing thus delays the formation of CtR upwash pairs and attenuates the vortex ejection rate from the wall. The near-wall residence time increases, as does the downwash-added skin-frictional drag. Moreover, the larger spacing of the CtR-CD pairs increases the ratio of the upwash/downwash region, incurring a larger low-momentum wake, and hence drag. This result is corroborated by direct skin-frictional measurements behind similar arrays in the controlled study of Godard and Stanislas.[19] Notwithstanding, the observed influence of spacing is relatively low compared with other parameters, in agreement with previous observations on CoR[11] and CtR arrays. [8,20]

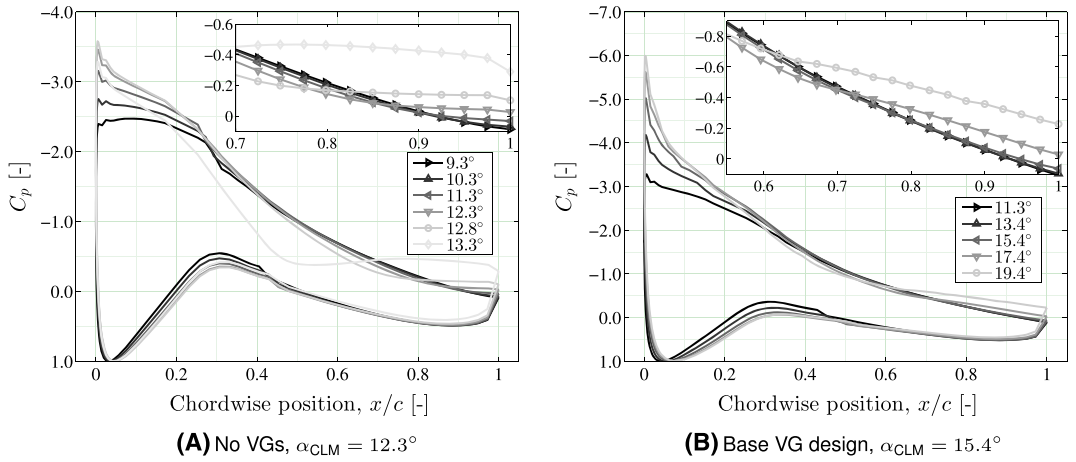

FIGURE 17 Pressure distribution for the airfoil in free transition with and without vortex generators (VGs). Complete distributions for angles of attack around maximum lift are illustrated together with suction side pressure details for the aft portions. NoVG, uncontrolled airfoil [Colour figure can be viewed at wileyonlinelibrary.com]

4 | LOADING DYNAMICS

During testing, the separation mode became increasingly intermittent in the post-stall region with VGs. For the uncontrolled airfoil, stall is preceded by a growing region of trailing edge separation. This is illustrated in the pressure distributions of Figure 17A. Note the reduction in C_p and gradual elongation of the pressure plateau as the flow separates. In contrast, for the 5 and 10 mm VGs, trailing edge separation does not appear before $C_l|_{max}$. However, beyond this critical point, the flow entered a state of vigorous separation/reattachment, observed with intermittently separated and (fully) attached pressure distributions. Figure 17B illustrates the temporal average of this phenomenon for the base VG design case. It is immediately notable that the aft pressure plateau is somewhat inclined, owing to the fluctuations between the stalled and attached conditions.

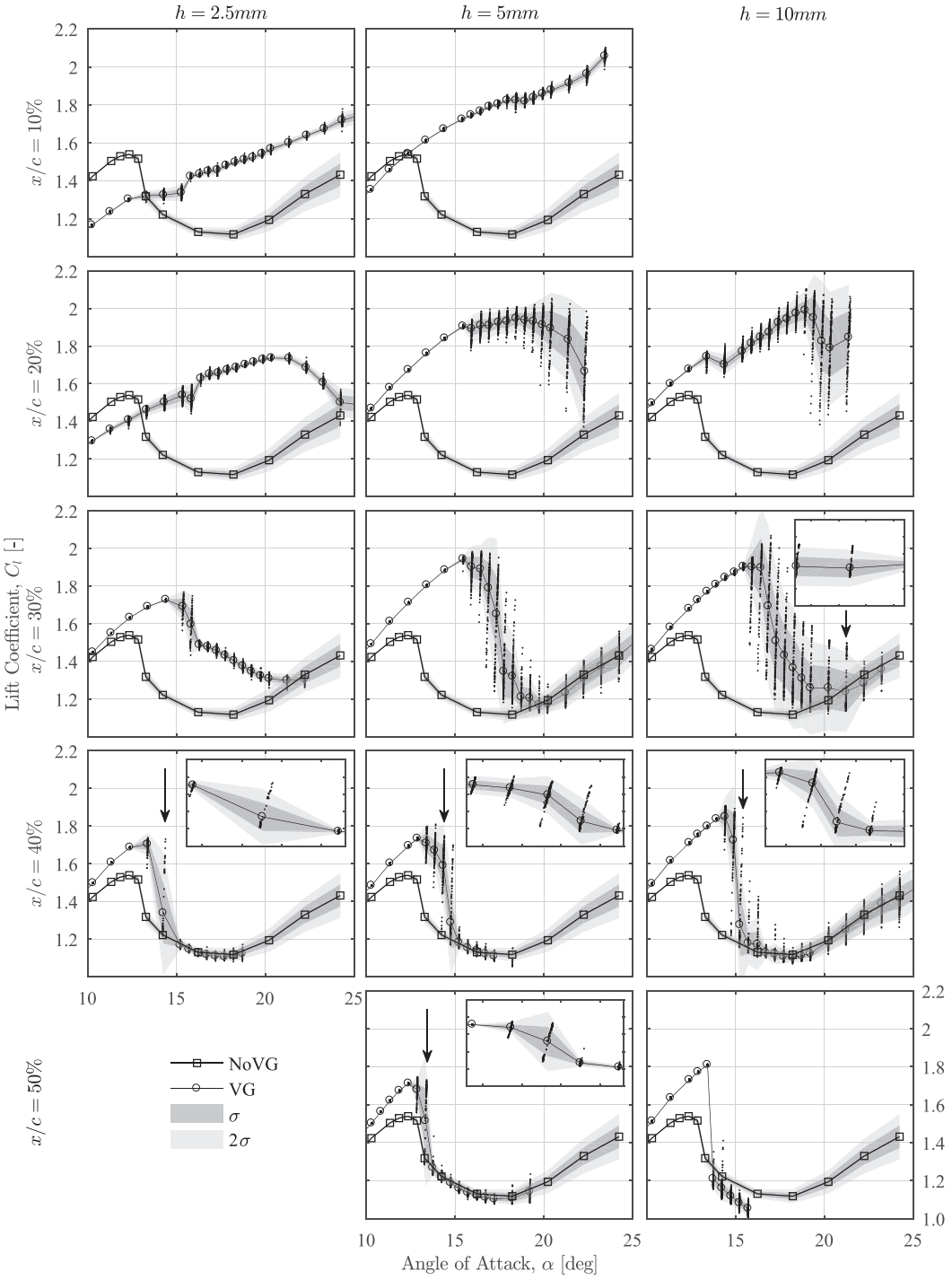

FIGURE 18 Lift fluctuations for the uncontrolled and controlled cases with different vortex generator (VG) heights and chordwise positions. The solid lines and symbols are time-averaged measurements. Scattered data points show all observations in the sample, and the shaded bounds indicate deviations from the mean. Inserts centred about indicated positions (arrows) indicate bimodal behaviour. NoVG, uncontrolled airfoil

The pressure samples were large enough to provide higher order lift statistics. Figure 18 compares lift polars of the clean airfoil with and without VGs, including the standard deviation σ. It is evident that separation dynamics intensify in the stalled regime of the controlled case. Moreover, bimodal behaviour was occasionally observed for all VG heights aft of the 20% chordwise mounting position. This occurred here just after $C_l|_{max}$, in contrast to Manolesos and Voutsinas,[9] who observed a "bifurcation" (or bimodality) at $C_l|_{max}$ of an 18% thick airfoil with VGs at 30% chord. Typical lift signatures displaying bimodality are illustrated in Figure 19, with stepwise amplitudes of approximately 20% to 30% of the low lift levels. Note that the angle at which this was observed varies with the inverse of the VG mounting position, similar to α_{CLM}. Additionally, since bimodality preferentially occurs for sharp stalling configurations, it is highly sensitive to the angle of attack. Therefore, experimentally, its detection depends on the precise settings of the model angle of attack. As postulated by Manolesos and Voutsinas,[9] this behaviour is probably linked to the motion of stall cells around the instrumented wing station.

The fluctuations for all VG height/chordwise combinations are synthesized in Figure 20. Fluctuations with VGs (σ_{VG}) are normalized by fluctuations in uncontrolled conditions (σ) for a given angle of attack; stronger load variations with VGs, ie, $\frac{\sigma_{VG}}{\sigma} > 1$, lie outside the shaded region. Note that the same measure (σ_{VG}) has been used for cases of bimodality, simply to illustrate the degree of the overall fluctuations. Broadly speaking, the fluctuations are stronger for larger VGs at more forward mounting positions. This also appears to hold in the prestall region for the 10-mm VGs. Practically, this implies that oversizing VGs to compensate for design uncertainties may aggravate turbine loading dynamics and fatigue damage.

These results appear to corroborate the early field test campaigns, which already hinted that VGs may alter the dynamic load behaviour of wind turbines.[8] Whilst the underlying mechanisms require deeper investigation, we offer a possible explanation based on the current findings and expe-

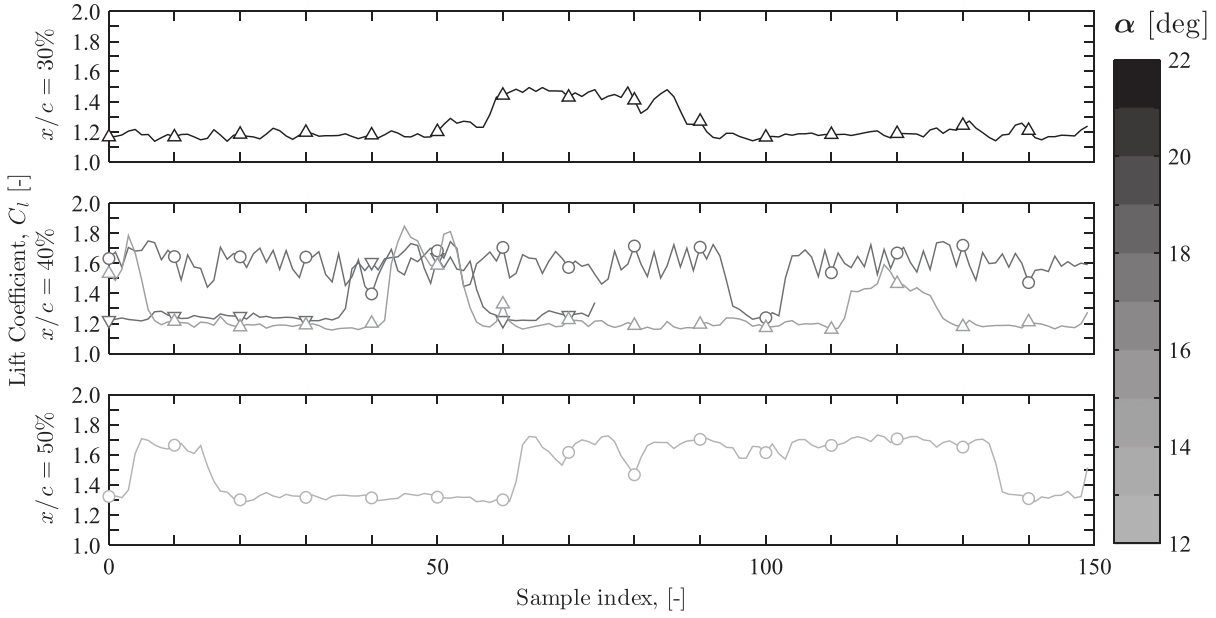

FIGURE 19 Lift signatures exhibiting bimodal behaviour for different vortex generator heights and chordwise positions, observed at different angles of attack. Symbols: $h = 2.5$ mm (▽); $h = 5$ mm (○); $h = 10$ mm (△)

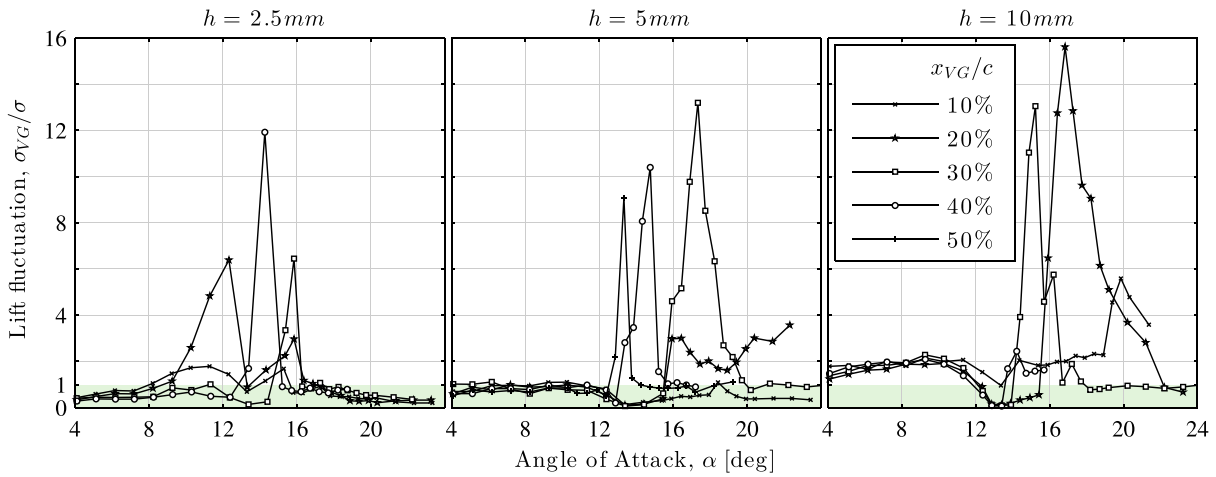

FIGURE 20 Lift fluctuation for controlled cases relative to the uncontrolled case. Data falling outside the shaded region indicates stronger fluctuations with vortex generators [Colour figure can be viewed at wileyonlinelibrary.com]

riences. For sufficiently large VGs, incipient separation aft of the VGs will be postponed. With increasing angle of attack, the APG will gradually shorten the effective range of the vortices. When the flow is eventually retarded close to the VGs, a highly unsteady process of separation and reattachment commences: The vortices are attenuated too quickly to prevent separation or are momentarily strong enough to enhance mixing over the airfoil and postpone it. This occurs until the separation point is sufficiently upstream of the VGs, such that they are rendered completely ineffective within the already separated boundary layer. At this point, the dynamics are less intermittent and the flow becomes "steadily" separated.

5 | CONCLUSIONS AND OUTLOOK

This article presents a wind tunnel sensitivity study of the DU97-W-300 airfoil to various VG designs. The goal was to map these sensitivities to understand the relative importance of the design variables, rather than optimizing the VG geometry for this specific case.

Qualitative OFVs were performed to gauge the overall influence of the VGs on the flow regime. A detailed analysis of the oil streaks in the presence of the wall-bounded vortices has shown good correspondence with theory and prior empirical knowledge. The indirect determination of the vortex strength using this simple experimental technique coupled with inviscid vortex theory also demonstrated a quantitative application of this experimental method.

The major VG parameters were then investigated using salient metrics such as the maximum lift coefficient and aerodynamic efficiency. The influence of the VG vane angle and length, displayed clear optima within the ranges tested ($\beta = \pm 12^{\circ}$, $L = 4h$), in general agreement with past experimental studies, but contrary to the linear relations often assumed or predicted by different fidelity models. A CtR, common downflow VG system with a CDA planform was superior to design variations such as a CoR array with delta vanes. On the other hand, the spanwise packing density displayed minimal influence on the metrics studied. The chordwise position of the VG array determines the control range of the streamwise vortices and, therefore, had the largest effect on the performance. The airfoil performance was also sensitive to variations in the vane height, which was considered in conjunction with the chordwise placement. However, larger VG heights (>1% chord) proved detrimental relative to smaller design variants.

The presence of a VG MS increased the base drag (+6%) and reduced the lift of the clean airfoil. The result cannot be generalized easily, as the severity of the effect depends on the specific airfoil's sensitivity to roughness. However, the higher this sensitivity, the larger the expected influence from the MS. Thus, in field operation, where roughened conditions prevail because of weathering, the effect of the MS will likely be lower. In this regard, the leading edge roughness sensitivity was also explored using ZZ tape. The VGs were able to offset the detrimental roughness effects, but the airfoil performance was still inferior to the clean-controlled case.

A consideration of the lift signal fluctuations revealed that the presence of VGs increased the dynamic loads in the delayed but eventual onset of the stall regime. This was pronounced for the larger VGs and forward mounting positions, reaching up to 16 times the fluctuations in the uncontrolled case. For larger VGs, higher fluctuations were induced throughout the operating envelope, not only in the stall regime.

Optimization of flow control devices ultimately requires knowledge of the environmental conditions of the specific application. For instance, the presence of spanwise wind turbine blade flows could make CoR arrays more attractive because of a lower sensitivity to inflow direction variations. Additionally, other performance metrics such as VG self-noise may be of importance when evaluating different designs. The results presented concern the performance of the DU97-W-300 airfoil and the numerous but limited set of VG design variables explored here. However, we expect that the observed relative importance of VG parameters can be generalized to other airfoils as well.

ACKNOWLEDGEMENTS

The authors would like to thank Stefan Bernardy and Leo Molenwijk for their expertise with the preparation of the model and operation of the wind tunnel, as well as Pranav Manjunath for assistance during the campaign. The constructive comments of the reviewers on the first draft of this paper are also sincerely appreciated. This work has been partially funded by the EU's FP7 AVATAR project, under the grant FP7-ENERGY-2013-1/no. 608396, and the Dutch TKI Wind op Zee D4REL project, grant number TKIW02007.

EXPERIMENTAL DATASET

The experimental data and supplementary graphs are publicly available via the 4TU Centre for Research Data (see Supplementary Material[34]).

ORCID

Daniel Baldacchino http://orcid.org/0000-0002-4515-237X
Delphine De Tavernier http://orcid.org/0000-0002-8678-8198

REFERENCES

1. Skrzypiński W, Gaunaa M, Bak C. The effect of mounting vortex fenerators on the DTU 10MW reference wind turbine blade. *J Phys Conf Ser*. 2014;524:012034.
2. Oerlemans S. Wind turbine noise: primary noise sources. Technical Report NLR-TP-2011-066, NLR; 2011.

3. Schubauer GB, Spangenberg WG. Forced mixing in boundary layers. *J Fluid Mech*. 1960;8:10-32.
4. Hoerner F, Borst HV. *Fluid-Dynamic Lift: Practical Information on Aerodynamic and Hydrodynamic Lift*. Brick Town, NJ: LA Hoerner; 1985.
5. Lengani D, Simoni D, Ubaldi M, Zunino P, Bertini F. Turbulent boundary layer separation control and loss evaluation of low profile vortex generators. *Exp Thermal Fluid Sci*. 2011;35(8):1505-1513.
6. Sullivan TL. Effect of vortex generators on the power conversion performance and structural dynamic loads of the Mod-2 wind turbine. Technical Report; 1984.
7. Antoniou I, Petersen SM, Øye S, Westergaard C. The ELKRAFT 1MW wind turbine: results from the test program. In: European Union Wind Energy Conference; 1996:251-255.
8. Griffin DA. Investigation of Vortex Generators for Augmentation of Wind Turbine Power Performance. Technical Report NREL/SR-440-21399, NREL; 1996.
9. Manolesos M, Voutsinas SG. Experimental investigation of the flow past passive vortex generators on an airfoil experiencing three-dimensional separation. *J Wind Eng Ind Aerodyn*. 2015;142:130-148.
10. Jones JP. The calculation of the paths of vortices from a system of vortex generators, and a comparison with experiment. Technical Report, A.R.C.; 1957.
11. Pearcey HH. Shock induced separation and its prevention by design and boundary layer control. In: Lachmann GV, ed. *Boundary Layer and Flow Control*. Oxford: Pergamon Press; 1961:1166-344.
12. Lögdberg O, Fransson JHM, Alfredsson PH. Streamwise evolution of longitudinal vortices in a turbulent boundary layer. *J Fluid Mech*. 2009;623:27-58.
13. Baldacchino D, Ferreira C, Ragni D, van Bussel GJW. Point vortex modelling of the wake dynamics behind asymmetric vortex generator arrays. *J Phys Conf Ser*. 2016;753(2).
14. Lögdberg O, Angele K, Alfredsson PH. On the robustness of separation control by streamwise vortices. *Eur J Mech B Fluids*. 2010;29(1):9-17.
15. Wendt BJ. Parametric study of vortices shed from airfoil vortex Generators. *AIAA J*. 2004;42(11):2185-2195.
16. Angele K, Muhammad-Klingmann B. The effect of streamwise vortices on the turbulence structure of a separating boundary layer. *Eur J Mech B Fluids*. 2005;24:539-554.
17. Ashill PR, Fulker JL, Hackett KC. A review of recent developments in flow control. *Aeronaut J*. 2005;109(1095):205-232.
18. Lin JC. Review of research on low-profile vortex generators to control boundary-layer separation. 2002;38(4-5):389-420.
19. Godard G, Stanislas M. Control of a decelerating boundary layer. Part 1: Optimization of passive vortex generators. *Aerosp Sci Technol*. 2006;10(3):181-191.
20. Fouatih OM, Medale M, Imine O, Imine B. Design optimization of the aerodynamic passive flow control on NACA 4415 airfoil using vortex generators. *Eur J Mech B Fluids*. 2016;56:82-96.
21. Gao L, Zhang H, Liu Y, Han S. Effects of vortex generators on a blunt trailing-edge airfoil for wind turbines. *Renewable Energy*. 2015;76:303-311.
22. Timmer WA, van Rooij RPJOM. Summary of the delft university wind turbine dedicated airfoils. *J Sol Energy Eng*. 2003;125:488-496.
23. van Rooij RPJOM. Modification of the boundary layer calculation in RFOIL for improved airfoil stall prediction. Technical Report IW-96087R, TU Delft, The Netherlands; 1996.
24. van Ingen JL. A suggested semi-empirical method for the calculation of the boundary layer transition region. Technical Report VTH-74, Delft University of Technology, Dept. of Aerospace Engineering, The Netherlands; 1956.
25. Westphal RV, Eaton JK, Pauley WR. Interaction between a vortex and a turbulent boundary layer in a streamwise pressure gradient. *Turbulent Shear Flows 5*. Ithaca, NY: Springer; 1987:266-277.
26. Baldacchino D, Manolesos M, Ferreira C, et al. Experimental benchmark and code validation for airfoils equipped with passive vortex generators. *J Phys Conf Ser*. 2016;753(2):022002.
27. White FM. *Viscous Fluid Flow*, 3rd ed. New York: McGraw Hill; 2006.
28. Drela M, Gilest MB. Viscous-inviscid analysis of transonic & low Reynolds number airfoils. *AIAA J*. 1987;25:1347-1355.
29. Holden H, Babinsky H. Effect of microvortex generators on separated normal shock/ boundary layer interactions. *J Aircr*. 2007;44(1):170-174.
30. Sørensen NN, Zahle F, Bak C, Vronsky T. Prediction of the effect of vortex generators on airfoil performance. *J Phys Conf Ser*. 2014;524(1):012019.
31. Velte CM, Hansen MOL, Okulov VL. Multiple vortex structures in the wake of a rectangular winglet in ground effect. *Exp Thermal Fluid Sci*. 2016;72:31-39.
32. Pauley WR, Eaton JK. Experimental study of the development of longitudinal vortex pairs embedded in a turbulent boundary layer. *AIAA J*. 1988;26(7):816-823.
33. Aparicio M, Martín R, Muñoz A, González A. AVATAR Deliverable 3.3: Results of a parametric study of flow devices, guidelines for design. Technical Report; 2016.
34. Baldacchino D. Experimental parameter study for passive vortex generators on a 30% thick airfoil. TU Delft Dataset. https://doi.org/10.4121/uuid:e2a3fa3c-dc19-4cad-9375-3124cf95f9c5; 2017.

How to cite this article: Baldacchino D, Ferreira C, De Tavernier D, Timmer WA, van Bussel GJW. Experimental parameter study for passive vortex generators on a 30% thick airfoil. *Wind Energy*. 2018;21:745–765. https://doi.org/10.1002/we.2191

APPENDIX A: POLARS

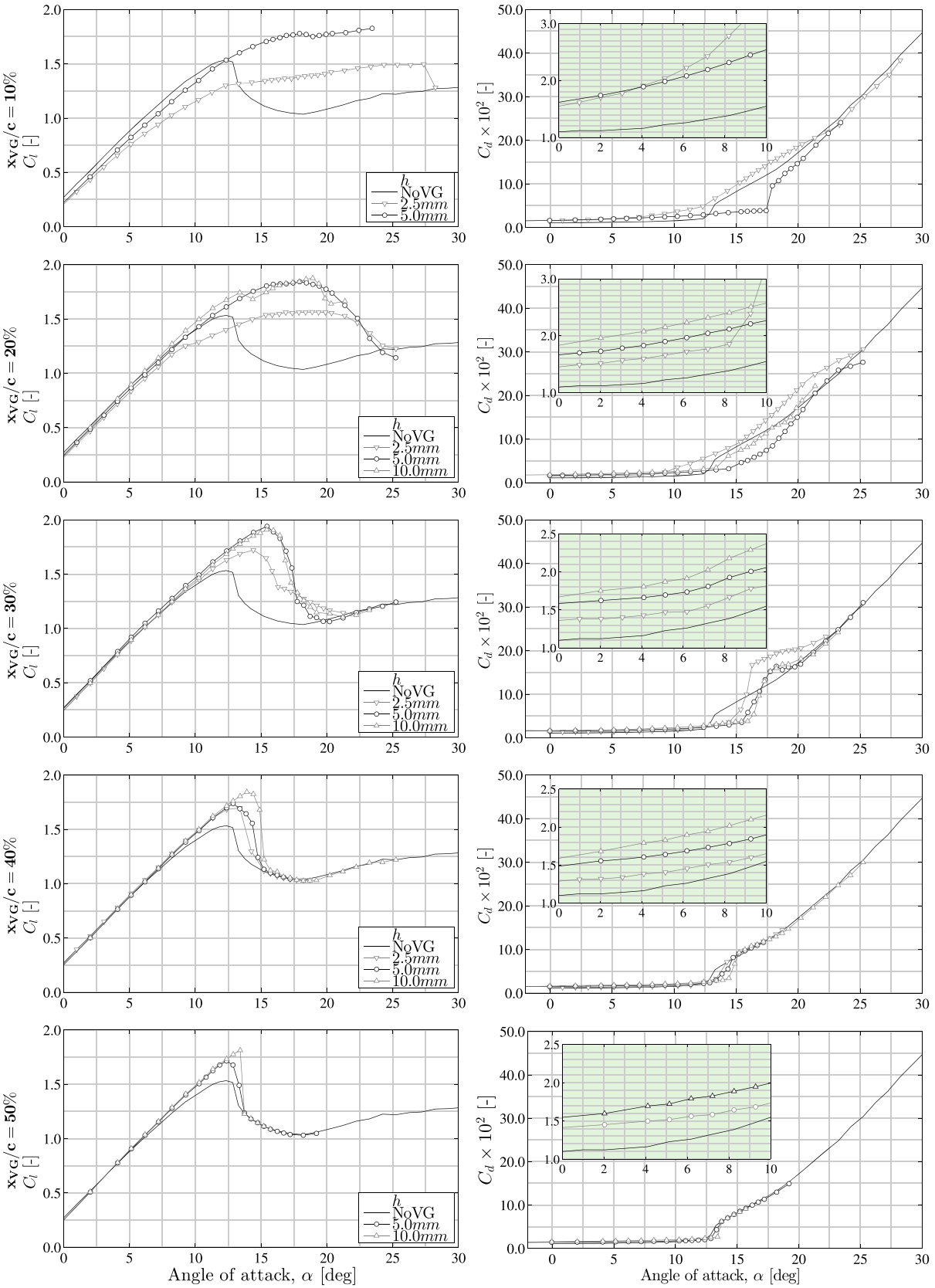

FIGURE A1 Sensitivity to array chordwise placement and vortex generator vane height. Graphs are grouped into rows according to the array chordwise placement (top-bottom): $x_{VG} = 10\%c$ to $50\%c$. NoVG, uncontrolled airfoil [Colour figure can be viewed at wileyonlinelibrary.com]

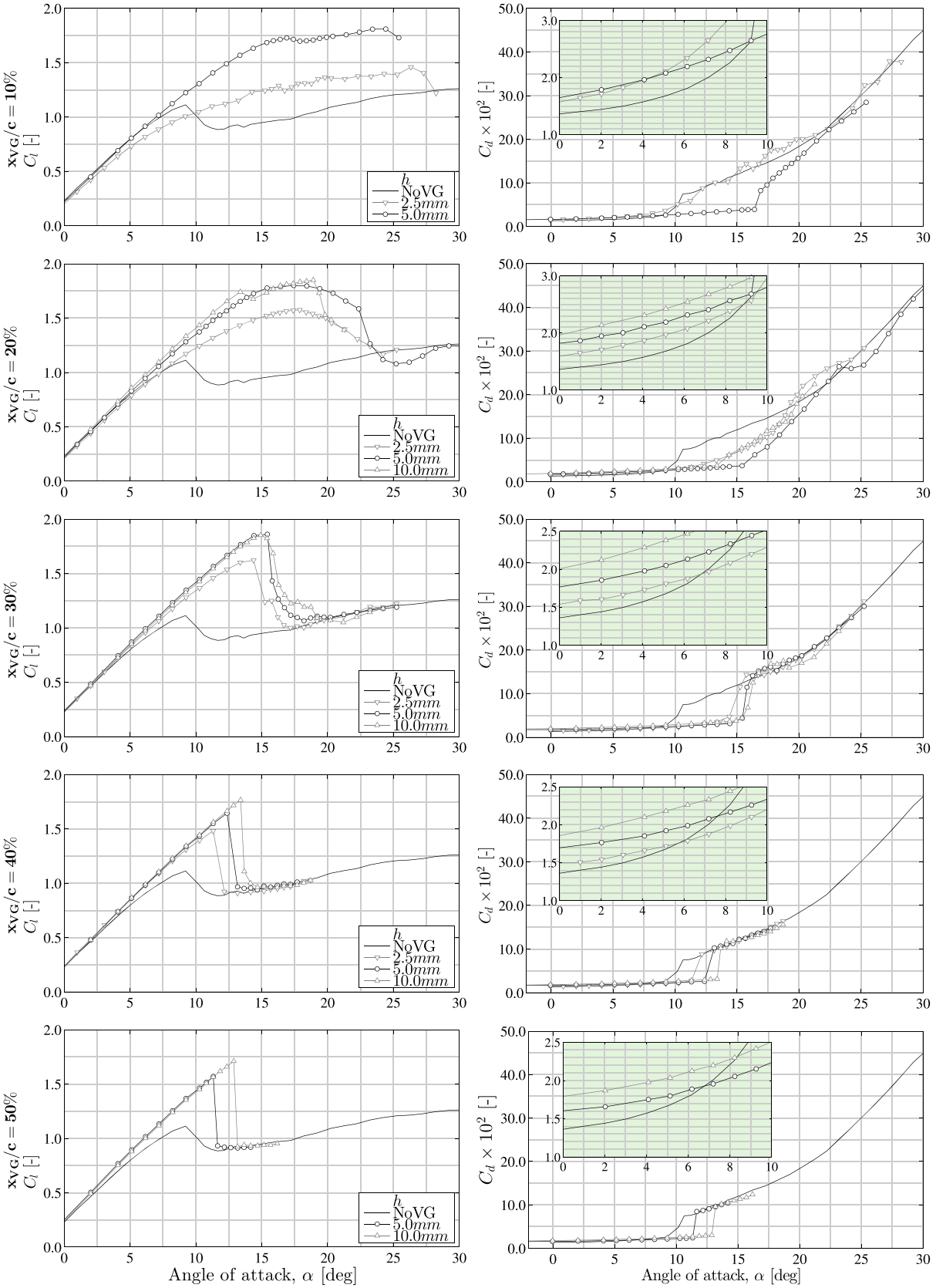

FIGURE A2 Same as Figure A1 for the tripped condition. CD, common downwash; CoR, corotating; CtR, counter-rotating; CU, common upwash; NoVG, uncontrolled airfoil [Colour figure can be viewed at wileyonlinelibrary.com]

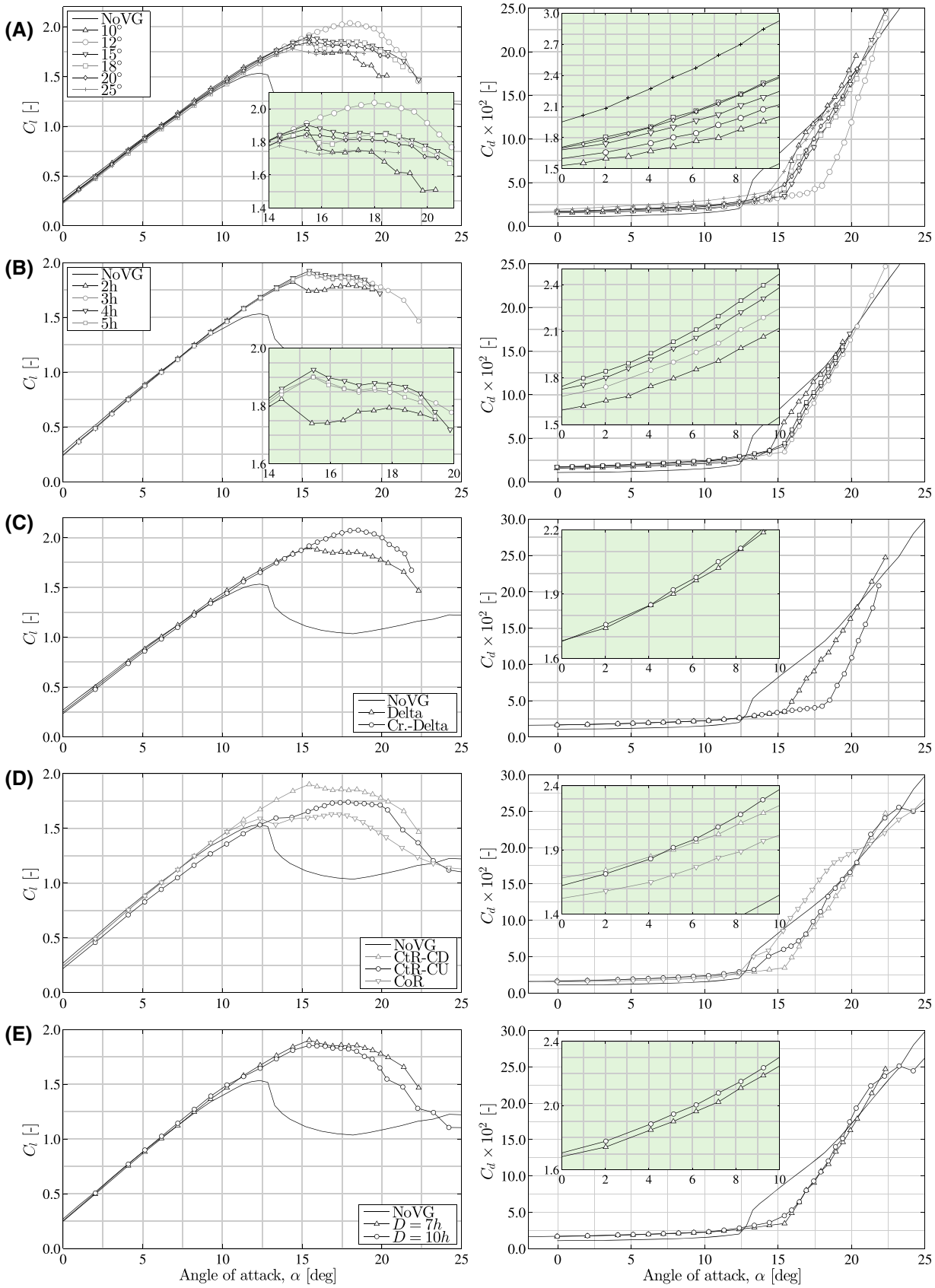

FIGURE A3 Airfoil performance sensitivity to the A, vane angle; B, vane length; C, vane shape; D, array configuration; and E, pair spacing. CD, common downwash; CoR, corotating; CtR, counter-rotating; CU, common upwash; NoVG, uncontrolled airfoil [Colour figure can be viewed at wileyonlinelibrary.com]